NASA
Technical
Paper
2559

April 1986

NASA-TP-2559 19860014088

Static Investigation of Two STOL Nozzle Concepts With Pitch Thrust-Vectoring Capability

Mary L. Mason and
James R. Burley II

NASA

NASA Technical Paper 2559

1986

Static Investigation of Two STOL Nozzle Concepts With Pitch Thrust-Vectoring Capability

Mary L. Mason and
James R. Burley II

Langley Research Center
Hampton, Virginia

National Aeronautics
and Space Administration

**Scientific and Technical
Information Branch**

SUMMARY

A static investigation of the internal performance of two short take-off and landing (STOL) nozzle concepts with pitch thrust-vectoring capability has been conducted in the static test facility of the Langley 16-Foot Transonic Tunnel. An axisymmetric concept consisting of a circular approach duct with a convergent-divergent nozzle was tested at dry and afterburning power settings. Pitch thrust vectoring was implemented by vectoring the approach duct without changing the nozzle geometry. A nonaxisymmetric (two-dimensional) convergent-divergent nozzle concept at dry and afterburning power settings was also tested. Pitch thrust vectoring was implemented by blocking the nozzle exit and deflecting a door in the lower nozzle flap. The nozzles were tested at nozzle pressure ratios up to 10.0, depending on model geometry. Results indicate that both pitch vectoring concepts produced resultant pitch vector angles which were nearly equal to the geometric pitch vector angles. The axisymmetric nozzle concept had only small thrust losses at the largest pitch deflection of 70°, but the two-dimensional convergent-divergent nozzle concept had considerable performance losses at both of the two pitch deflection angles tested, 60° and 70°.

INTRODUCTION

Current tactical fighter aircraft are designed with high-performance propulsion systems for maximum maneuverability over a large range of flight Mach numbers and engine throttle settings. The tactical fighter of the future will certainly require a similar high level of propulsion-exhaust system performance during cruise and maneuvering and will probably require short take-off and landing (STOL) capability. Reducing the runway length requirements of fighter aircraft would result in more effective and efficient base locations, decreased mission sortie distances, and improved aircraft survivability in bomb-damaged environments (refs. 1 and 2). Future advanced fighter designs could be adapted for STOL capability by augmenting the propulsion-exhaust system with advanced thrust-vectoring exhaust nozzles (refs. 2 to 5). Vectoring the engine thrust during take-off or landing would provide additional lift control and reduce the aircraft ground roll with only a minimal increase in the total aircraft size and weight. For example, the Harrier, a current tactical aircraft, has been successfully designed for STOL and vertical take-off and landing (VTOL) capabilities by use of nozzle thrust vectoring, and it also uses thrust vectoring for improved maneuverability during forward flight (ref. 6).

Two basic types of exhaust-nozzle geometries are under consideration for the tactical fighter of the future: the axisymmetric (or round) nozzle concept and the nonaxisymmetric (or rectangular) nozzle concept. Axisymmetric nozzles are widely used in established fighter aircraft propulsion systems (refs. 4, 7, and 8) and typically demonstrate high levels of nozzle internal performance. Nonaxisymmetric nozzles, notably the two-dimensional convergent-divergent (2-D C-D) nozzle and the single-expansion-ramp nozzle (SERN), also show high nozzle internal performance levels which are comparable to performance levels of axisymmetric nozzles (refs. 9 and 10). In addition, the rectangular geometry of nonaxisymmetric nozzle concepts is simpler to modify for thrust vectoring than the axisymmetric nozzle geometry and facilitates airframe integration in both vectored-thrust and forward-thrust flight modes. Extensive studies of isolated nonaxisymmetric nozzle geometries at static conditions (no external flow), summarized in reference 11, have shown that selected

nonaxisymmetric nozzles can be successfully modified to include thrust vectoring in the longitudinal (pitch) plane and in the lateral (yaw) plane with little loss of basic nozzle internal performance.

As part of a continuing study to develop STOL vectoring nozzle concepts (refs. 1, 2, 3, and 5), an investigation has been conducted in the static test facility of the Langley 16-Foot Transonic Tunnel. Two basic nozzle types were tested at static conditions to investigate the effects of longitudinal, or pitch, thrust vectoring on nozzle internal performance. One basic nozzle type consisted of an axisymmetric convergent-divergent nozzle located downstream of a circular approach duct. Pitch thrust vectoring was implemented by varying the approach duct geometry without changing the nozzle geometry. The other basic nozzle type was a nonaxisymmetric 2-D C-D nozzle with pitch thrust vectoring implemented by blocking the nozzle exit and opening a door in the lower nozzle flap. For each of the two basic nozzle types, unvectored configurations representative of dry and afterburning power settings and vectored configurations representative of dry power settings were tested to simulate realistic nozzle operating conditions. The effect of approach duct geometry on the performance of the unvectored forward-flight axisymmetric nozzle was also considered during this test. The results of this investigation are presented in this report as nozzle-internal-performance parameters (discharge coefficient, internal thrust ratio, and resultant thrust ratio) and resultant pitch vector angles. Results from this static investigation were also published in reference 12.

SYMBOLS

All forces (except resultant gross thrust) and resultant vector angles are referred to the model body axis (measured from model centerline). A detailed discussion of the data-reduction and calibration procedures as well as definitions of forces, angles, and propulsion relations used in this report can be found in reference 13.

A_e nozzle exit area, in^2

A_e/A_t nozzle expansion ratio

A_t nozzle geometric throat area (minimum internal area), in^2

F measured thrust along body axis, lbf

F_i ideal isentropic gross thrust, $w_p\sqrt{\frac{RT_{t,j}}{g^2}\left(\frac{2\gamma}{\gamma - 1}\right)\left(1 - \frac{p_\infty}{p_{t,j}}\right)^{(\gamma-1)/\gamma}}$, lbf

F_N measured normal force, lbf

F_r resultant gross thrust, $\sqrt{F^2 + F_N{}^2 + F_S{}^2}$, lbf

F_S measured side force, lbf

g acceleration due to gravity, 32.174 ft/sec^2

h internal height of nozzle cross section used to define transition-section internal geometry for 2-D C-D nozzles (see figs. 10, 11, 13, and 15), in.

h_e nozzle exit height, in.

l axial distance from nozzle attachment point to cross section used to define the transition-section internal geometry for 2-D C-D nozzles (see figs. 10, 11, 13, and 15), in.

l_n axial length of 2-D C-D nozzle from nozzle attachment point to nozzle exit, in.

$p_{t,j}$ jet total pressure, psi

p_∞ ambient pressure, psi

R gas constant, 1716 ft^2/sec^2 for air

r corner radius of nozzle cross section used to define the transition-section internal geometry for 2-D C-D nozzles (see figs. 10, 11, 13, and 15), in.

$T_{t,j}$ jet total temperature, °R

w_i ideal weight-flow rate, lbf/sec

w_p measured weight-flow rate, lbf/sec

w_p/w_i nozzle discharge coefficient

γ ratio of specific heats, 1.3997 for air

δ_p resultant pitch thrust-vector angle, $\tan^{-1}\frac{F_N}{F}$, deg

$\delta_{v,p}$ geometric pitch thrust-vector angle measured from model centerline (positive for downward deflection angles), deg

ε nozzle divergence angle, deg

Abbreviations:

A/B afterburning

C-D convergent-divergent

Conf. configuration

NPR nozzle pressure ratio, $p_{t,j}/p_\infty$

$(NPR)_{des}$ design nozzle pressure ratio (NPR for fully expanded flow at nozzle exit)

Sta. model station, in.

STOL short take-off and landing

2-D two-dimensional

Configuration Designations:

CDAD	axisymmetric C-D nozzle with approach duct
CDAD-A1, CDAD-A2	axisymmetric A/B-power C-D nozzle configurations with approach ducts
CDAD-D1, CDAD-D2, ..., CDAD-D4	axisymmetric dry-power C-D nozzle configurations with approach ducts
TD-A1, TD-A2, ..., TD-A4	nonaxisymmetric A/B-power 2-D C-D nozzle configurations
TD-D1, TD-D2, ..., TD-D4	nonaxisymmetric dry-power 2-D C-D nozzle configurations
U-0	straight approach duct with $\delta_{v,p} = 0°$
V	general designation for counterrotating approach ducts
V-0	counterrotating approach duct with $\delta_{v,p} = 0°$
V-35	counterrotating approach duct with $\delta_{v,p} = 35°$
V-70	counterrotating approach duct with $\delta_{v,p} = 70°$

APPARATUS AND METHODS

Static Test Facility

This investigation was conducted in the static test facility of the Langley 16-Foot Transonic Tunnel. Testing in this facility is conducted in a large room where the jet from a simulated single-engine propulsion system exhausts to atmosphere through a large, open doorway. A control room is remotely located from the test area, and a closed-circuit television is used to observe the model when the jet is operating. The static test facility uses the same clean, dry air supply as that of the 16-Foot Transonic Tunnel and has a similar air control system which incorporates a heat exchanger to maintain the jet flow at a constant stagnation temperature.

Single-Engine Propulsion Simulation System

A sketch of the single-engine air-powered nacelle model on which the test nozzles were installed is presented in figure 1. The propulsion simulation system is shown with an axisymmetric nozzle configuration mounted for testing. The body shell forward of station 20.50 was removed for this test.

An external high-pressure air system provided a continuous flow of clean, dry air maintained at a stagnation temperature of about 530°R. During propulsion simulation this high-pressure air was varied up to about 10 atm. The pressurized air was transported by six air lines through a high-pressure plenum chamber. The air was then discharged perpendicularly into the model low-pressure plenum through eight multiholed sonic nozzles equally spaced around the high-pressure plenum. (See

fig. 1.) This airflow system was designed to minimize any forces on the balance generated by the transfer of axial momentum as the air is passed from the nonmetric high-pressure plenum to the metric (attached to the balance) circular low-pressure plenum. Two flexible metal bellows seal the air system between the metric and nonmetric sections of the model and compensate for axial forces caused by pressurization. The pressurized air then flows from the circular low-pressure plenum, through a choke plate and a circular instrumentation section, and finally into the installed nozzle configuration. Each test configuration was attached to the instrumentation section at model station 40.20. (See fig. 1.)

Nozzle Design

Two basic nozzle concepts were tested during this investigation. The first concept consisted of an axisymmetric C-D nozzle installed at the end of a circular approach duct. The second concept was a 2-D C-D nozzle with a built-in transition from circular to rectangular geometry. These nozzle concepts were designed for installation on a low-bypass-ratio afterburning turbofan engine. The bypass fan flow and the engine core exhaust flow would, by design, mix together to exit through a single variable-area nozzle. Discussions of this engine configuration with descriptions of necessary power-plant modifications for pitch thrust vectoring are given in references 2, 3, and 12.

Axisymmetric nozzle configurations.- The axisymmetric nozzle configurations consisted of an approach duct which was installed at the end of the model instrumentation section (Sta. 40.20) and a C-D nozzle which was installed downstream of the duct. Pitch thrust vectoring was accomplished by deflecting only the approach duct without changing the nozzle geometry. Two approach-duct geometries were tested with C-D nozzles representing dry-power and A/B-power operational modes. A sketch of a simple circular duct geometry (approach duct U-0) is presented in figure 2. This duct was tested with the axisymmetric dry-power C-D nozzle (CDAD-D1) and with the axisymmetric A/B-power C-D nozzle (CDAD-A1). Sketches and geometric parameters defining the geometry of the two C-D nozzles are also presented in figure 2. A photograph of approach duct U-0 with the dry-power nozzle installed on the single-engine propulsion simulation system is shown in figure 3. This "straight," or "clean," approach duct was designed for axial thrust only and was not adaptable for pitch thrust vectoring. It was tested to provide a baseline duct geometry for determining any effects of more complex duct geometry on nozzle internal performance of unvectored ($\delta_{v,p} = 0°$) configurations.

A second approach duct with a more complex geometry than approach duct U-0 was also tested with the axisymmetric C-D nozzles. This duct simulated a counter-rotating duct design which could provide pitch thrust-vector angles $\delta_{v,p}$ from 0° to 70° (refs. 2, 3, and 12). Duct geometries simulating pitch thrust-vector angles of 0° (V-0), 35° (V-35), and 70° (V-70) were tested. The unvectored duct V-0 was tested with both the dry-power and A/B-power C-D nozzles. The two vectored ducts were tested only with the dry-power C-D nozzle. Sketches of the unvectored approach duct V-0 with the dry-power C-D nozzle (CDAD-D2) and with the A/B-power C-D nozzle (CDAD-A2) are presented in figure 4. A photograph of approach duct V-0 with the A/B-power C-D nozzle installed for testing is shown in figure 5. Sketches of approach duct V-35 with the dry-power C-D nozzle (CDAD-D3) are presented in figure 6, and a photograph of configuration CDAD-D3 is shown in figure 7. A sketch and a photograph of approach duct V-70 with the dry-power C-D nozzle (CDAD-D4) are shown in figures 8 and 9, respectively.

The V approach-duct geometry is a fixed-geometry representation of a complex variable-geometry duct (duct upstream of the nozzle) composed of two counterrotating duct sections. The V-0 approach duct represented the forward-thrust, or cruise, setting (undeflected) of the two movable sections. For pitch thrust vectoring, the two sections rotate in opposite directions (counterrotate) to deflect the downstream section down (in pitch) while the upstream section is kept correctly aligned at the approach duct attachment point. As a result, the nozzle attached at the downstream end of the approach duct is deflected in pitch away from the horizontal centerline. Approach duct V-35 represented an intermediate rotation of the two counterrotating sections, and approach duct V-70 represented a maximum counterrotation setting. Sketches of the V-35 duct-nozzle configuration CDAD-D3 in figure 6 present details showing the geometry of the two counterrotating sections in deflection. The counterrotating-duct geometry is based on a series of designs developed for vertical take-off and landing. More detailed explanations and discussions of the counterrotating-duct hardware are given in references 2, 3, and 12.

Nonaxisymmetric nozzle configurations.- The nonaxisymmetric nozzles of this investigation were 2-D C-D nozzles. The 2-D C-D nozzle is a nonaxisymmetric exhaust system with symmetric upper and lower sets of convergent and divergent flaps; the sidewalls have flat internal surfaces (ref. 14). At design nozzle pressure ratios $(NPR)_{des}$, all exhaust-flow expansion takes place inside the nozzle. The 2-D C-D nozzle internal geometry can be easily varied to set different operating power settings and nozzle expansion ratios.

The 2-D C-D nozzles considered during this test consisted of four dry-power nozzle configurations and four A/B-power nozzle configurations. Only the dry-power nozzles were adapted for pitch thrust-vectoring capability. The variations in nozzle geometry were tested to simulate realistic nozzle operating conditions and also to investigate the effects of nozzle expansion ratio A_e/A_t on nozzle performance at both dry and A/B power settings. Sketches of two dry-power 2-D C-D unvectored ($\delta_{v,p} = 0°$) nozzles (TD-D1 and TD-D2) are presented in figure 10. Sketches of two dry-power 2-D C-D pitch-vectored nozzles (TD-D3 with $\delta_{v,p} = 60°$ and TD-D4 with $\delta_{v,p} = 70°$) are presented in figure 11. A photograph of TD-D4 on the test model is presented in figure 12. Sketches of the maximum A/B-power 2-D C-D nozzle TD-A1 are presented in figure 13, and a photograph of this nozzle installed for testing is shown in figure 14. The four dry-power 2-D C-D nozzle configurations and nozzle configuration TD-A1 were designed for static testing only. Figure 15 presents sketches of three A/B-power 2-D C-D nozzles (TD-A2, TD-A3, and TD-A4) which were designed for additional testing on a wind tunnel aircraft model following this static investigation. (See ref. 15.) For compatibility with the wind tunnel model, these three nozzles were constructed with a smaller model scale (from a full-scale nozzle) than configuration TD-A1 or the dry-power 2-D C-D nozzles. In addition, each of these smaller scale nozzles was constructed with a smooth, faired external geometry to facilitate installation and integration into the wind tunnel model. A circular adaptor was required to install the smaller scale nozzles on the test apparatus, and a sketch of the adaptor is shown in figure 15(c). A photograph of uninstalled nozzles TD-A2, TD-A3, and TD-A4 is shown in figure 16.

The dry-power 2-D C-D nozzles and the A/B-power nozzle TD-A1 were each assembled from a set of fixed sidewalls and two sets of convergent-divergent flap segments (one upper flap set, one lower flap set). Each of the three small-scale A/B-power nozzles (TD-A2, TD-A3, and TD-A4) was cast as a single piece of hardware. (See fig. 16.) All the 2-D C-D nozzles had a built-in flow transition from circular (axisymmetric) at the engine and propulsion-simulator-system exhaust plane (Sta. 40.20) to rectangular (nonaxisymmetric) upstream of the nozzle convergence section. (See figs. 10, 11,

13, and 15.) The convergent-flap section caused a flow contraction followed by a flow expansion in the two-dimensional passage formed by the divergent-flap section.

These test nozzles were fixed-geometry representations of realistic full-scale nozzles with convergent-divergent flap segments which are mechanically linked for precise symmetrical movement as nozzle expansion ratio or throat area is increased or decreased (refs. 2, 3, and 12). To initiate thrust deflection in a realistic full-scale nozzle, the downstream face of the convergent section would slide toward the nozzle exit to block the normal jet flow path through the rear of the nozzle. As the nozzle exit becomes blocked, a deflector door would open up in the lower nozzle flap to provide a flow path for pitch thrust vectoring or for thrust spoiling. (See fig. 11(a) and details of the deflector door shown in fig. 11(b).) Only a lower-door deflection to a maximum of 70° for pitch vectoring was tested during this investigation. Opening an upper door simultaneously with the deflection of the lower door to deflection angles greater than 90° could provide thrust-reversing capability for deceleration or maneuvering.

Instrumentation

A six-component strain-gauge balance was used to measure forces and moments on the model downstream of model station 20.50 (metric break location). Jet total pressure was measured at a fixed location in the model with a seven-probe rake positioned upstream of the test configurations. (See fig. 1.) A thermocouple was positioned near the total-pressure rake to measure the jet total temperature. The flow rate of the high-pressure air supplied to the nozzle configurations was determined from pressure and temperature measurements in the high-pressure plenum calibrated with standard axisymmetric Stratford nozzles with known performance.

Data Reduction

All data were recorded simultaneously on magnetic tape. Approximately 50 frames of data, acquired at a rate of 10 frames per second, were used for each data point. Averaged values of data were used in computations. Data were always taken in order of increasing $p_{t,j}$. All force data in this report are referenced to the model centerline with the exception of resultant gross thrust F_r.

The basic nozzle performance parameters used in the presentation of results are internal thrust ratio F/F_i, resultant thrust ratio F_r/F_i, discharge coefficient w_p/w_i, and resultant pitch thrust-vector angle δ_p. The internal thrust ratio F/F_i is the ratio of the actual measured thrust along the body axis to the ideal nozzle thrust. Ideal thrust F_i is computed from measured weight-flow rate w_p, jet total pressure $p_{t,j}$, and jet total temperature $T_{t,j}$. (See definition of F_i in "Symbols" section.) Measured nozzle thrust along the body axis F was obtained from the balance axial-force measurement with corrections included for model weight tares and balance interactions. Additional corrections to F were necessary to eliminate bellows tares. Although the bellows arrangement in the air pressurization system was designed to eliminate any pressure and momentum interactions with the balance, small bellows tares on all six balance components still existed. These tares resulted from a small difference in pressure between the ends of the bellows when internal velocities within the air system were high. Additional bellows tares resulted from small differences between the forward-bellows and aft-bellows spring constants during bellows pressurization. The bellows tares were determined by testing standard axisymmetric Stratford calibration nozzles with known performance over

a range of model loads expected from the test nozzle configurations. The resulting tares were then applied to the balance data to obtain the corrected thrust F along the body axis. The procedure for computing the bellows tares and for correcting the balance data is discussed in detail in reference 13.

The resultant thrust ratio F_r/F_i is the resultant gross thrust F_r normalized by the ideal gross thrust F_i. Resultant thrust is computed from corrected values of axial-, normal-, and side-force balance measurements. By definition, differences between F/F_i and F_r/F_i occur when the exhaust flow is directed (vectored) away from the axial direction. Axial thrust F is diminished by thrust vectoring whereas resultant thrust F_r may not decrease, since F_r includes longitudinal and lateral force components. Resultant pitch thrust-vector angle δ_p reflects the degree of exhaust-flow turning produced by the various pitch thrust-vectoring configurations.

The final parameter used in the presentation of results is nozzle discharge coefficient w_p/w_i, the ratio of measured weight-flow rate to ideal weight-flow rate. Ideal isentropic weight-flow rate w_i is computed from the jet total pressure $p_{t,j}$, jet total temperature $T_{t,j}$, and the measured nozzle throat area. The nozzle discharge coefficient reflects the weight-flow capability of a nozzle and is reduced by momentum and vena contracta losses (ref. 16).

PRESENTATION OF RESULTS

The basic nozzle internal performance data obtained during this investigation are presented in figures 17 to 20. Comparison and summary plots of the results are presented in figures 21 to 26. The data figures are organized as follows:

RESULTS AND DISCUSSION

Axisymmetric Nozzle Configurations

The results of the axisymmetric nozzle (CDAD) configurations are summarized in figures 21 to 23. Figure 21 presents the effects of varying the approach-duct geometry on the unvectored ($\delta_{v,p} = 0°$) dry-power CDAD configurations, and figure 22 gives similar results for the A/B-power CDAD configurations. Results are shown as nozzle discharge coefficient w_p/w_i and resultant thrust ratio F_r/F_i presented as functions of nozzle pressure ratio (NPR).

The duct-nozzle configurations showed the same general trends in F_r/F_i with NPR regardless of duct geometry. At values of NPR below design ($(NPR)_{des}$), the C-D nozzles were operating overexpanded, and overexpansion losses (which are due to internal flow separation and to an exit static pressure lower than ambient) typically cause lower values of F_r/F_i. Nozzle separation is diminished as NPR increases to $(NPR)_{des}$, and thus F_r/F_i increases with increasing NPR. Resultant thrust ratio F_r/F_i reaches peak values at NPR $\approx (NPR)_{des}$. For higher values of NPR (above $(NPR)_{des}$), F_r/F_i decreases from peak values through underexpansion losses.

Both the dry-power and the A/B-power configuration showed the same effects of unvectored-duct geometry on w_p/w_i and F_r/F_i. Duct geometry had no effect on w_p/w_i. The F_r/F_i data showed only a small effect of duct geometry. Values of F_r/F_i were decreased by use of the more complex counterrotating duct V-0, but this loss was generally less than 1 percent. The losses in F_r/F_i because of the V-0 duct geometry were largest for values of NPR below design, when the nozzle flow is overexpanded. As NPR increased, the losses in F_r/F_i because of duct geometry decreased such that at NPR > $(NPR)_{des}$, there was very little effect of duct geometry on F_r/F_i. These differences in F_r/F_i probably resulted from internal flow separation and total-pressure distortion caused by the complex wall geometry of approach duct V-0.

The effects on nozzle internal performance of pitch vectoring through approach-duct deflection are summarized in figure 23. Resultant pitch vector angle δ_p is presented to show turning efficiency and resultant thrust ratio F_r/F_i is presented to show nozzle performance. The values of δ_p produced by the counterrotating-duct pitch vectoring configuration were very close to the geometric pitch vector angles $\delta_{v,p}$. The F_r/F_i data showed no effect of pitch vectoring on nozzle performance for $\delta_{v,p} = 35°$ but showed up to a 2.5-percent loss for $\delta_{v,p} = 70°$. Discharge-coefficient data, presented in figure 18, also showed a loss of about 2.5 percent for the V-70 configuration but showed no loss for the V-35 configuration.

The internal geometry of approach duct V-35 was fairly regular with a moderate flow-path angle. (See fig. 6.) Approach duct V-35 (as well as ducts V-0 and V-70) had a decreasing duct internal cross-sectional area distribution (decreasing from duct attachment point to nozzle attachment point), which tends to reduce internal flow separation (ref. 17). Because of the moderate flow-path angle and the decreasing internal-area distribution, separation in approach duct V-35 was probably minimal and, consequently, there were no further reductions in F_r/F_i or changes in w_p/w_i from the results of the unvectored V-0 configuration. Approach duct V-70, however, had extremely sharp and steep internal corners caused by the large internal flow-path angle. (See fig. 8.) Although the geometric pitch vector angle measured from the centerline of the internal flow path was 70°, the lower duct wall actually

had a flow-turning angle near 90°. This severe internal geometry probably resulted in a large region of separated flow in the duct and also in the nozzle and produced subsequent losses in F_r/F_i and w_p/w_i. As NPR increased, separation continued in the duct but probably diminished in the nozzle, so that nozzle performance F_r/F_i for the V-70 configuration increased to the same levels as the V-0 and V-35 configurations at NPR > 4.0. Discharge-coefficient data for approach duct V-70, however, remained about 2.5 percent lower than w_p/w_i values for the approach ducts V-0 or V-35, regardless of NPR. This loss in w_p/w_i indicates an effective-area decrease in the duct, probably due to flow separation. As NPR increased, the loss in weight-flow rate w_p remained in the V-70 duct-nozzle system, even though the nozzle recovered to the same F_r/F_i performance levels as the V-0 and V-35 configurations at the higher NPR's. Although the loss in w_p equated to an actual thrust (i.e., F_r) loss, losses in weight-flow rate w_p and discharge coefficient w_p/w_i were not reflected in the value of resultant thrust ratio F_r/F_i. As noted previously, ideal isentropic gross thrust F_i is based on actual measured weight-flow rate w_p; any reduction in weight-flow rate affects both F_r and F_i and is subsequently cancelled out of the ratio F_r/F_i.

In summary, deflecting the approach duct to provide nozzle pitch thrust vectoring was effective in generating large values of δ_p but, for a 70° thrust-vector angle, resulted in reduced discharge coefficients at all NPR's and in internal performance losses at low NPR's. However, at typical design operating NPR, nozzle internal performance losses were small.

Nonaxisymmetric Nozzle Configurations

The results of the nonaxisymmetric 2-D C-D nozzle configurations are summarized in figures 24 to 26. Effects of nozzle expansion ratio A_e/A_t and throat area A_t are presented in figure 24 for the unvectored dry-power 2-D C-D nozzles and in figure 25 for the A/B-power 2-D C-D nozzles. Increasing A_e/A_t had no effect on nozzle discharge coefficient w_p/w_i for the dry-power 2-D C-D nozzles (fig. 24). Similarly, increasing A_e/A_t had essentially no effect on w_p/w_i for the A/B-power 2-D C-D nozzles (compare data for TD-A3 and TD-A4 in fig. 25), but increasing A_t did affect w_p/w_i. The values of w_p/w_i for configuration TD-A1 (A_t = 11.58 in^2) were about 1 percent higher than those of configuration TD-A4 (A_t = 4.17 in^2), even though both nozzles had the same expansion ratio of 1.50 and the same internal geometry upstream of the throat (except for nozzle scale).

Variation of w_p/w_i with A_t was not expected for these nozzles. All three A/B-power 2-D C-D nozzles in figure 25 had the same internal geometry upstream of the throat, although configuration TD-A1 had a different model scale than TD-A3 and TD-A4. The smaller nozzles (TD-A3 and TD-A4) were preceded by a circular adaptor (see fig. 15(c)), but the adaptor was not expected to affect the nozzle performance characteristics. A possible explanation of the unexpected effect of A_t on w_p/w_i is the effect of model scale and upstream duct length on the internal boundary layer along the nozzle walls (ref. 18).

Because of increased flow-path length (approximately 4 in.), passing the exhaust flow through the adaptor section before it entered the nozzle could have possibly thickened the boundary layer in the nozzle so that the internal boundary-layer thickness of configuration TD-A4 was greater than the boundary-layer thickness of configuration TD-A1, which did not use the adaptor. As a result, the ratio of effective internal flow area to geometric internal flow area for configuration TD-A1 would have

been greater than that for configuration TD-A4. Proportionally, TD-A1 would have then passed more weight flow and thus had larger discharge coefficients than TD-A4. Even if the adaptor had no effect on boundary-layer thickness and the boundary-layer thicknesses were the same for the two nozzles, the boundary layer of configuration TD-A4 would have comprised a larger proportion of the total internal flow area than the boundary layer of TD-A1 (because of the difference in A_t between TD-A1 and TD-A4). As a result, configuration TD-A1 would have had proportionally larger effective flow area than configuration TD-A4 and subsequently would have had higher discharge coefficients.

The trends in resultant thrust ratio F_r/F_i which occurred for both power setting geometries are typical of the effects of expansion ratio on 2-D C-D nozzle performance reported in earlier studies (refs. 14, 19, and 20). Increasing A_e/A_t increases the design nozzle pressure ratio NPR, thus causing peak F_r/F_i performance to occur at a higher value of NPR. In general, increasing A_e/A_t also increases nozzle overexpansion losses at lower values of NPR and decreases nozzle underexpansion losses at higher values of NPR. Thus, the low-expansion-ratio nozzles showed higher F_r/F_i performance at low NPR's (NPR < 4.0 for the dry-power nozzles and NPR < 6.0 for the A/B-power nozzles) and lower performance at higher NPR's than did the high-expansion-ratio nozzles.

Throat area had only a small effect on performance of A/B-power nozzles. (Compare data for TD-A4 and TD-A1 in fig. 25.) Configuration TD-A1 had lower performance than configuration TD-A4 at low NPR's (NPR < 3.50), where the nozzles were operating overexpanded. Although these configurations were supposed to be identical except for scale, small differences in effective internal area could have resulted from the possible differences in boundary-layer growth discussed earlier or from actual small differences in divergent-flap geometry which occurred in construction. These differences in effective flow area or actual internal geometry would have affected the location of shock-induced separation at these low NPR's and thus could have caused the small differences in F_r/F_i shown in figure 25.

Figure 26 summarizes the effects of pitch thrust vectoring on internal performance for the dry-power 2-D C-D nozzle configurations. As in figure 23, results are presented as δ_p and F_r/F_i as functions of NPR. The δ_p results indicated good flow turning, with values of δ_p actually larger than geometric pitch vector angle $\delta_{v,p}$. However, losses of 3 to 6 percent for F_r/F_i occurred at both $\delta_{v,p} = 60°$ and 70° over the entire NPR range tested. Thrust losses could have resulted from several internal geometry characteristics of the 2-D C-D vectoring nozzles. The flow-path length opened by the vectoring door could have been too short for large amounts of flow turning without internal flow separation. Blocking the nozzle exit (see fig. 11) created an internal surface which could also have caused internal flow separation or circulation effects resulting in thrust losses. In addition to the thrust losses, large losses in discharge coefficient w_p/w_i (from 5 to 10 percent) also occurred with pitch vectoring. (See figs. 19(b) to 19(d).) Decreases in discharge coefficient of this magnitude could result in adverse back-pressure effects on the engine (i.e., engine stall) during pitch thrust-vectoring operation.

In summary, pitch thrust vectoring of 2-D C-D nozzle flow by blocking the nozzle exit and deflecting a door in the lower nozzle surface produced large resultant pitch vector angles but had adverse effects on nozzle internal performance. A similar pitch thrust-vectoring configuration for convergent nozzles (ref. 21) which used a rotating lower door but did not block the normal nozzle exit produced good flow

turning with only small performance losses. Thus, it is possible that most of the performance losses measured for the 2-D C-D pitch vectoring configuration of this report are associated with blocking the nozzle exit.

CONCLUSIONS

An investigation has been conducted in the static test facility of the Langley 16-Foot Transonic Tunnel to determine the forward-thrust nozzle performance and the pitch thrust-vectoring effects of two short take-off and landing (STOL) nozzle concepts. One concept was an axisymmetric convergent-divergent nozzle located downstream of a circular approach duct with pitch thrust vectoring accomplished by deflecting the duct. The other concept was a two-dimensional (nonaxisymmetric) convergent-divergent nozzle with a door in the lower nozzle flap deflected for pitch thrust vectoring. Geometries representing both dry-power and afterburning-power operating modes were tested. Effects of unvectored-duct geometry and of pitch thrust vectoring were considered for the axisymmetric configurations. Effects of nozzle expansion ratio, throat area, and pitch thrust vectoring were considered for the two-dimensional convergent-divergent configurations. During testing, nozzle pressure ratio was varied up to about 10.0, depending on nozzle geometry. Results of this investigation can be summarized as follows:

1. At forward-thrust conditions, the approach-duct geometry had little or no effect on nozzle internal performance of the axisymmetric nozzle configurations.

2. For the axisymmetric nozzle configurations, pitch vectoring the approach duct at 35° and 70° produced resultant pitch vector angles equal to the geometric vector angles, with only small performance losses at the geometric pitch vector angle of 70°.

3. Pitch vectoring the two-dimensional convergent-divergent nozzle flow by blocking the conventional nozzle exit and opening up a vectoring door in the lower flap surface produced resultant pitch vector angles which were greater than the geometric pitch vector angles. This pitch vectoring configuration resulted in large internal performance losses at both geometric pitch vector angles of 60° and 70°.

NASA Langley Research Center
Hampton, VA 23665-5225
February 11, 1986

REFERENCES

1. Lewis, G. M.; and Lewis, W. J.: V/STOL Status From the Engine Technology Viewpoint. AIAA-81-2648, Dec. 1981.

2. Curry, Steven G.; Barnes, G. Ray; Jones, Thomas J.; and Hartill, William R.: Exhaust Nozzle Concepts for STOL Tactical Aircraft. AIAA-83-1226, June 1983.

3. Tape, R. F.; Hartill, W. R.; Curry, S.; and Jones, T. J.: Vectoring Exhaust Systems for STOL Tactical Aircraft. 83-GT-212, American Soc. Mech. Eng., Mar. 1983.

4. Richey, G. K.; Surber, L. E.; and Berrier, B. L.: Airframe-Propulsion Integration for Fighter Aircraft. AIAA-83-0084, Jan. 1983.

5. Sotheran, A.: Development of Thrust Augmentation Technology for the Pegasus Vectored Thrust Engine. SAE 1982 Transactions, Volume 91, Soc. Automot. Eng., Inc., c.1983, pp. 4303-4311. (Available as SAE Paper 821390.)

6. Fozard, John W., compiler: The Jet V/STOL Harrier - An Evolutionary Revolution in Tactical Air Power. Aircraft Group, British Aerospace, c.July 1978.

7. Berrier, Bobby L.; and Maiden, Donald L.: Effect of Nozzle-Exhaust Flow on the Longitudinal Aerodynamic Characteristics of a Fixed-Wing, Twin-Jet Fighter Airplane Model. NASA TM X-2389, 1971.

8. Berrier, Bobby L.; and Re, Richard J.: Investigation of Convergent-Divergent Nozzles Applicable to Reduced-Power Supersonic Cruise Aircraft. NASA TP-1766, 1980.

9. Capone, Francis J.: The Nonaxisymmetric Nozzle - It Is for Real. AIAA Paper 79-1810, Aug. 1979.

10. Capone, Francis J.; and Berrier, Bobby L.: Investigation of Axisymmetric and Nonaxisymmetric Nozzles Installed on a 0.10-Scale F-18 Prototype Airplane Model. NASA TP-1638, 1980.

11. Leavitt, Laurence D.: Summary of Nonaxisymmetric Nozzle Internal Performance From the NASA Langley Static Test Facility. AIAA-85-1347, July 1985.

12. Barnes, G. R.; Curry, S. G.; and Wood, A. C.: Vectoring Exhaust Nozzle Technology. AIAA-84-1175, June 1984.

13. Capone, Francis J.: Static Performance of Five Twin-Engine Nonaxisymmetric Nozzles With Vectoring and Reversing Capability. NASA TP-1224, 1978.

14. Mason, Mary L.; and Berrier, Bobby L.: Static Investigation of Several Yaw Vectoring Concepts on Nonaxisymmetric Nozzles. NASA TP-2432, 1985.

15. Berndt, D. E.; Glidewell, R.; and Barnes, G. R.: Integration of Vectoring Nozzles in a STOL Transonic Tactical Aircraft. AIAA-85-1285, July 1985.

16. Shapiro, Ascher H.: The Dynamics and Thermodynamics of Compressible Fluid Flow. Volume I. Ronald Press Co., c.1953.

17. Burley, James R., II; and Carlson, John R.: Circular-to-Rectangular Transition Ducts for High-Aspect Ratio Nonaxisymmetric Nozzles. AIAA-85-1346, July 1985.

18. Berrier, Bobby L.; Leavitt, Laurence D.; and Bangert, Linda S.: Operating Characteristics of the Multiple Critical Venturi System and Secondary Calibration Nozzles Used for Weight-Flow Measurements in the Langley 16-Foot Transonic Tunnel. NASA TM-86405, 1985.

19. Berrier, Bobby L.; and Re, Richard J.: Effect of Several Geometric Parameters on the Static Internal Performance of Three Nonaxisymmetric Nozzle Concepts. NASA TP-1468, 1979.

20. Re, Richard J.; and Leavitt, Laurence D.: Static Internal Performance Including Thrust Vectoring and Reversing of Two-Dimensional Convergent-Divergent Nozzles. NASA TP-2253, 1984.

21. Leavitt, Laurence D.: Static Internal Performance of a Two-Dimensional Convergent Nozzle With Thrust-Vectoring Capability up to 60°. NASA TP-2391, 1985.

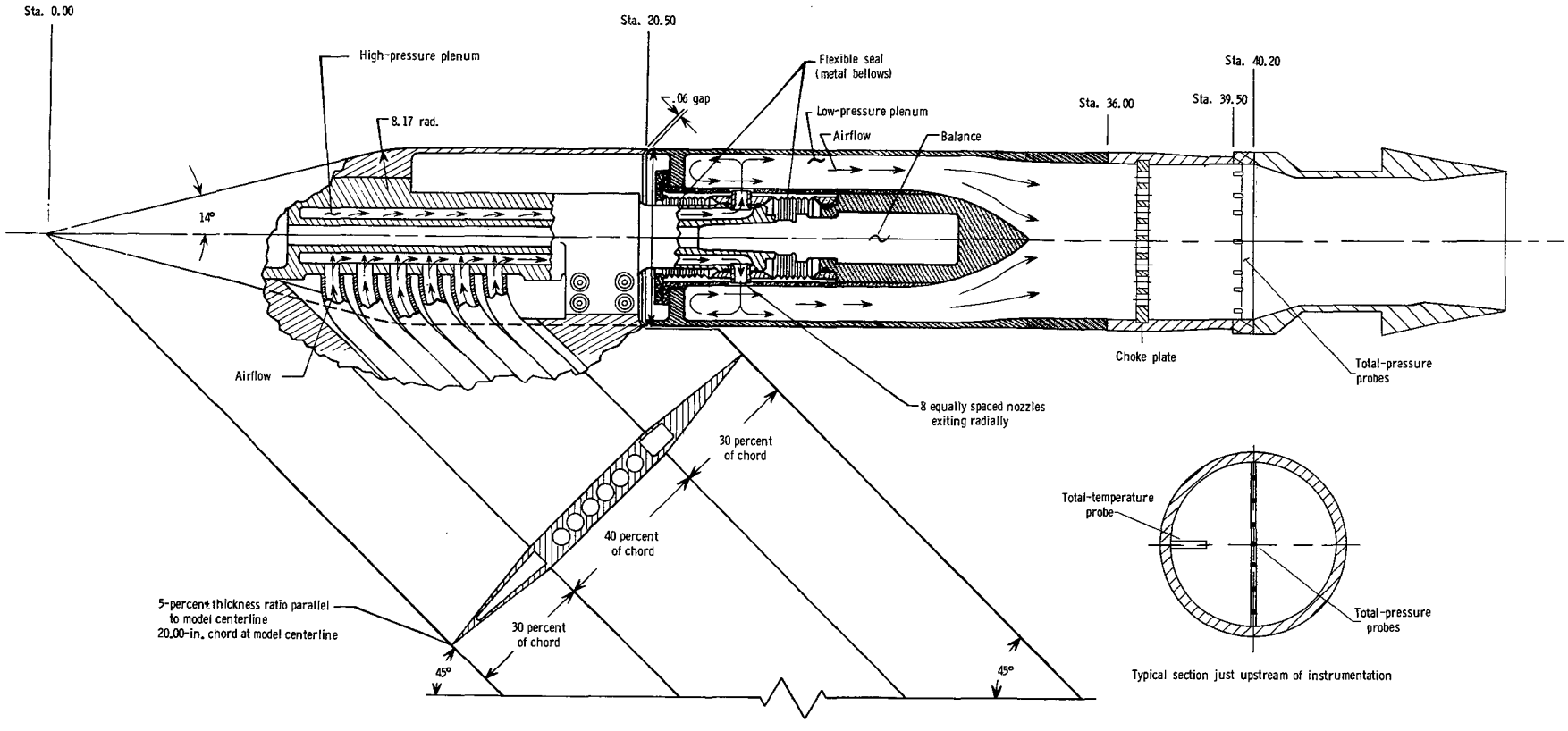

Figure 1.- Air-powered propulsion simulation system with a typical test nozzle installed. Linear dimensions are in inches.

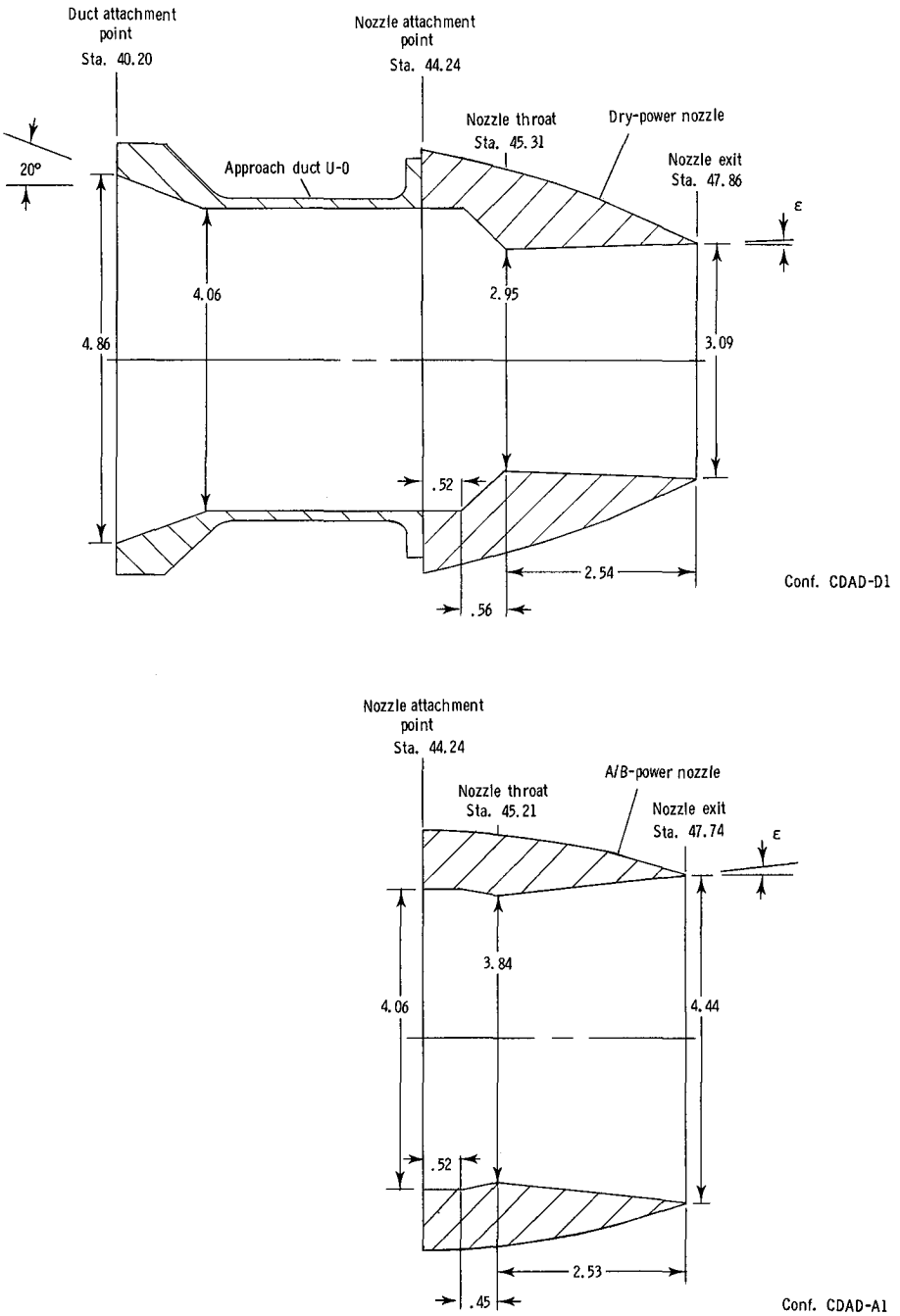

Configuration	Power Setting	A_e/A_t	A_t, in^2	$(NPR)_{des}$	ε, deg	$\delta_{v,p}$, deg
CDAD-D1	Dry	1.10	6.82	3.06	1.60	0
CDAD-A1	A/B	1.34	11.57	4.95	6.80	0

Figure 2.- Axisymmetric C-D nozzles with approach duct U-0 (straight duct geometry with $\delta_{v,p} = 0°$). Linear dimensions are in inches.

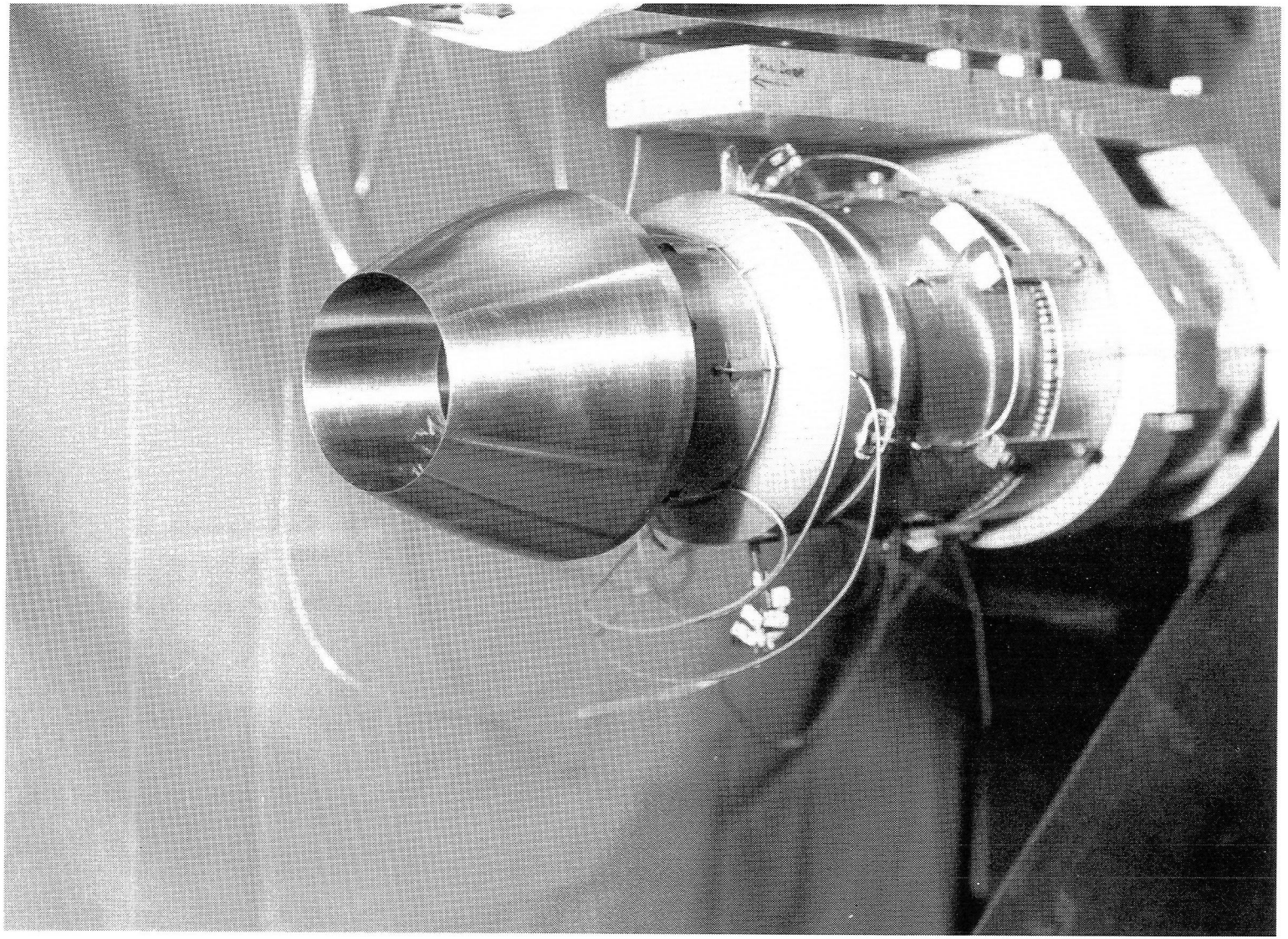

L-86-309

Figure 3.- Dry-power C-D nozzle configuration CDAD-D1 (with approach duct U-0) installed on single-engine propulsion simulation system.

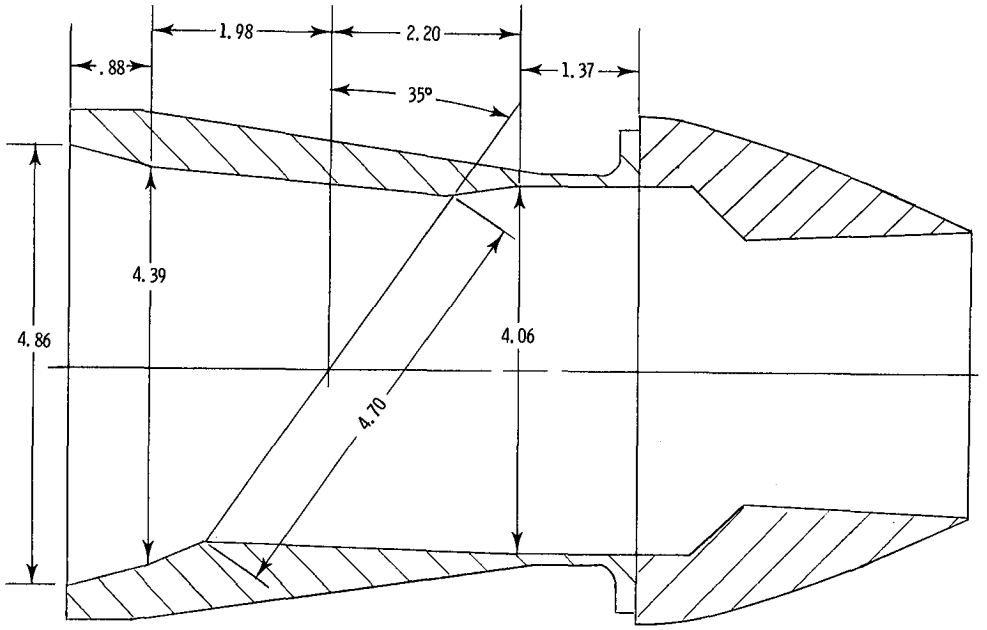

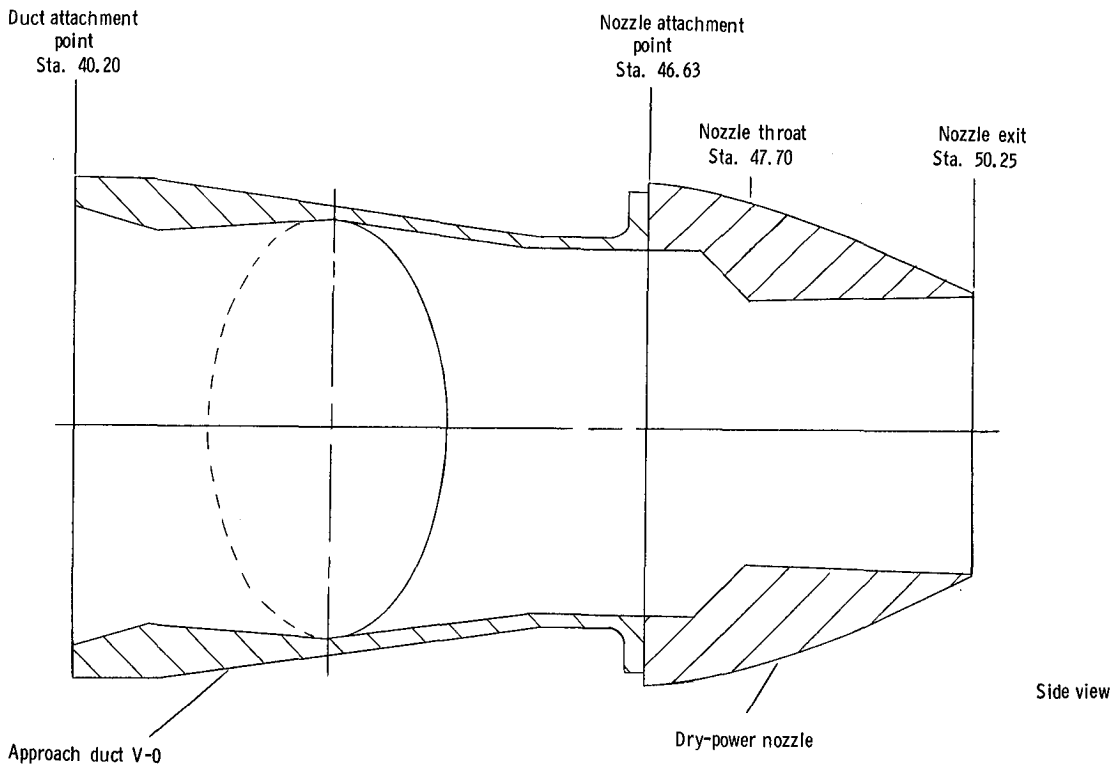

(a) Configuration CDAD-D2 (dry-power nozzle).

Figure 4.- Convergent-divergent nozzles with approach duct V-0 (counterrotating-duct geometry with $\delta_{v,p} = 0°$). See figure 2 for nozzle geometry details. Linear dimensions are in inches.

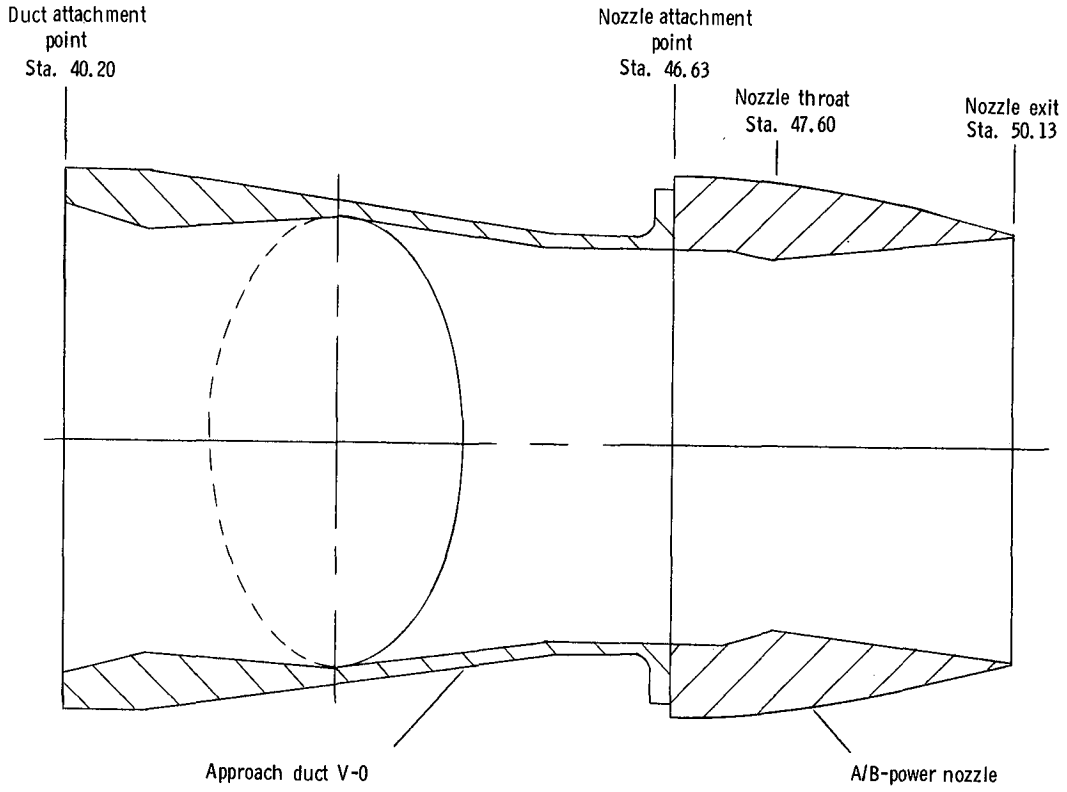

(b) Configuration CDAD-A2 (A/B-power nozzle).

Figure 4.- Concluded.

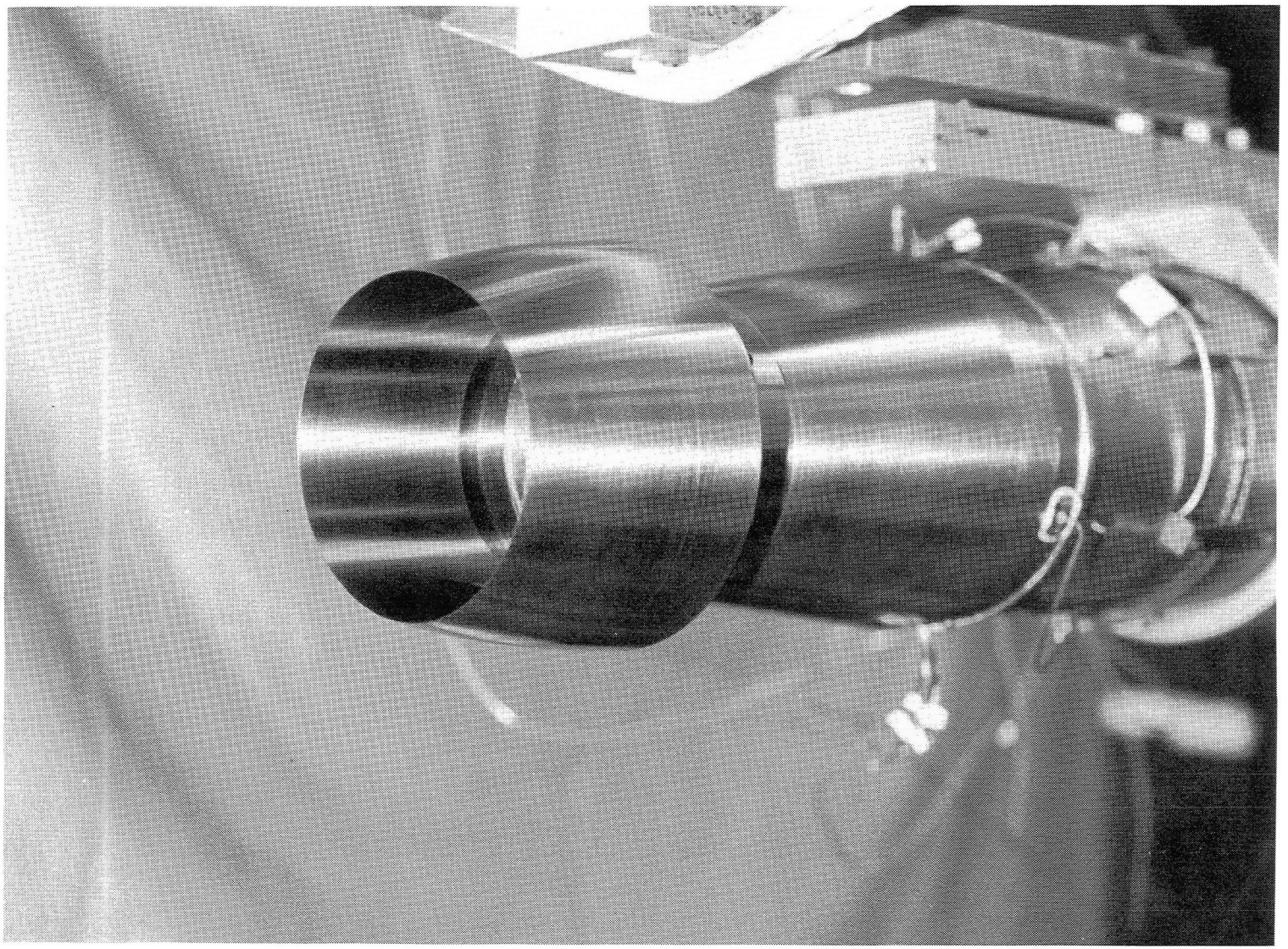

L-86-310

Figure 5.- A/B-power C-D nozzle configuration CDAD-A2 (with approach duct V-0) installed on single-engine propulsion simulation system.

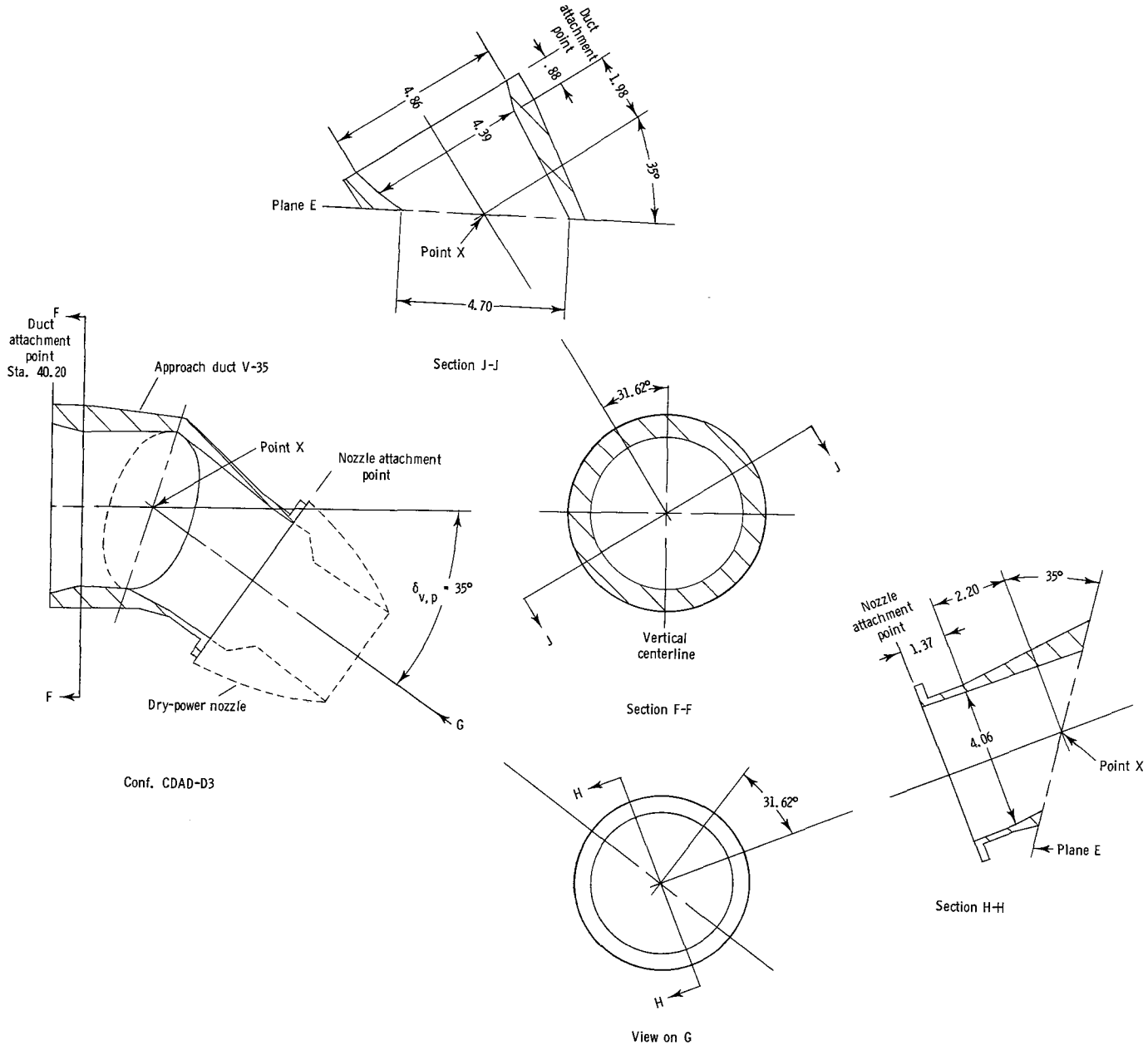

Figure 6.- Dry-power C-D nozzle with approach duct V-35 (counterrotating-duct geometry with $\delta_{v,p}$ = 35°). See figure 2 for nozzle geometry details. Linear dimensions are in inches.

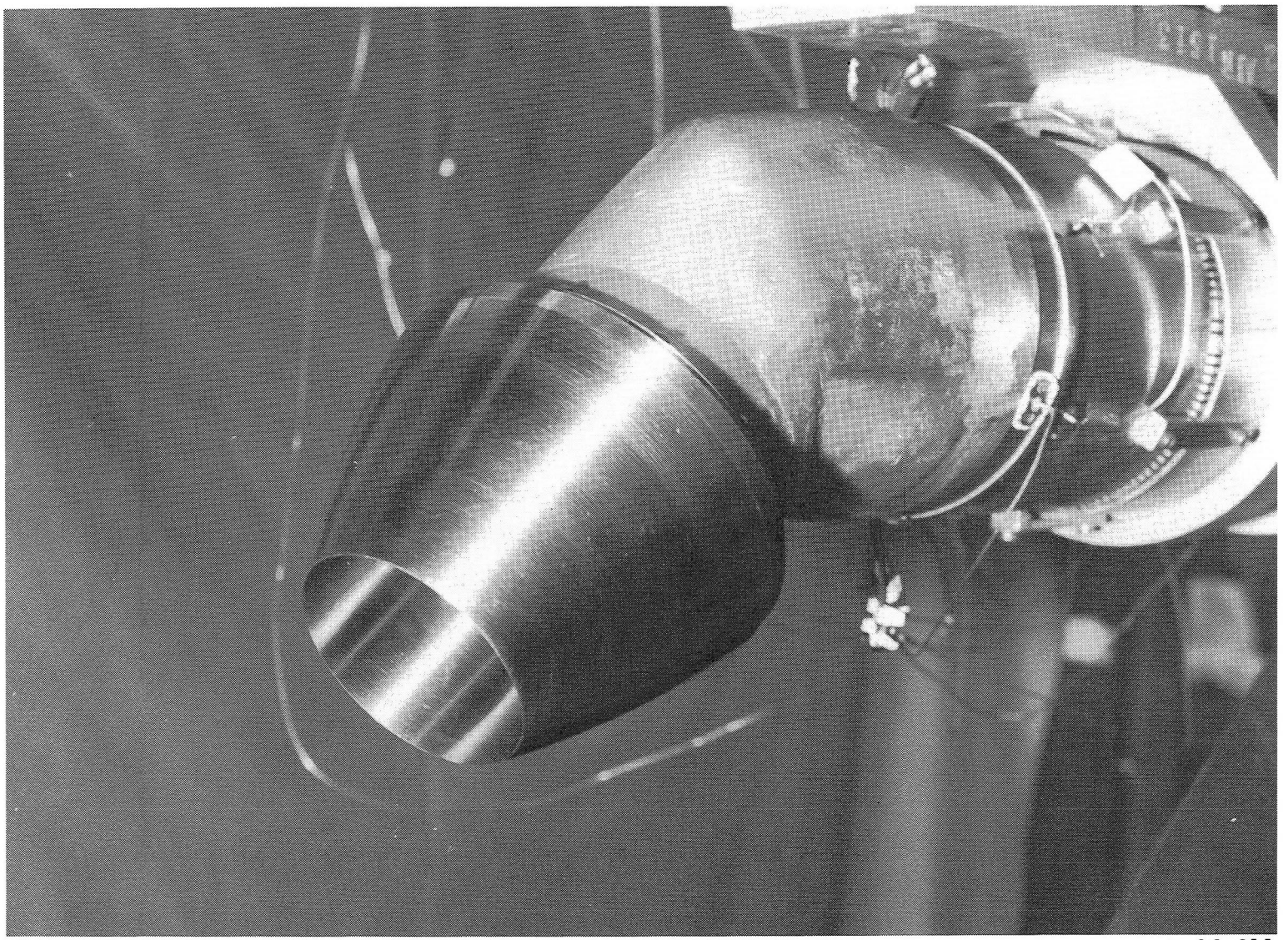

L-86-311

Figure 7.- Dry-power C-D nozzle configuration CDAD-D3 (with approach duct V-35) installed on single-engine propulsion simulation system.

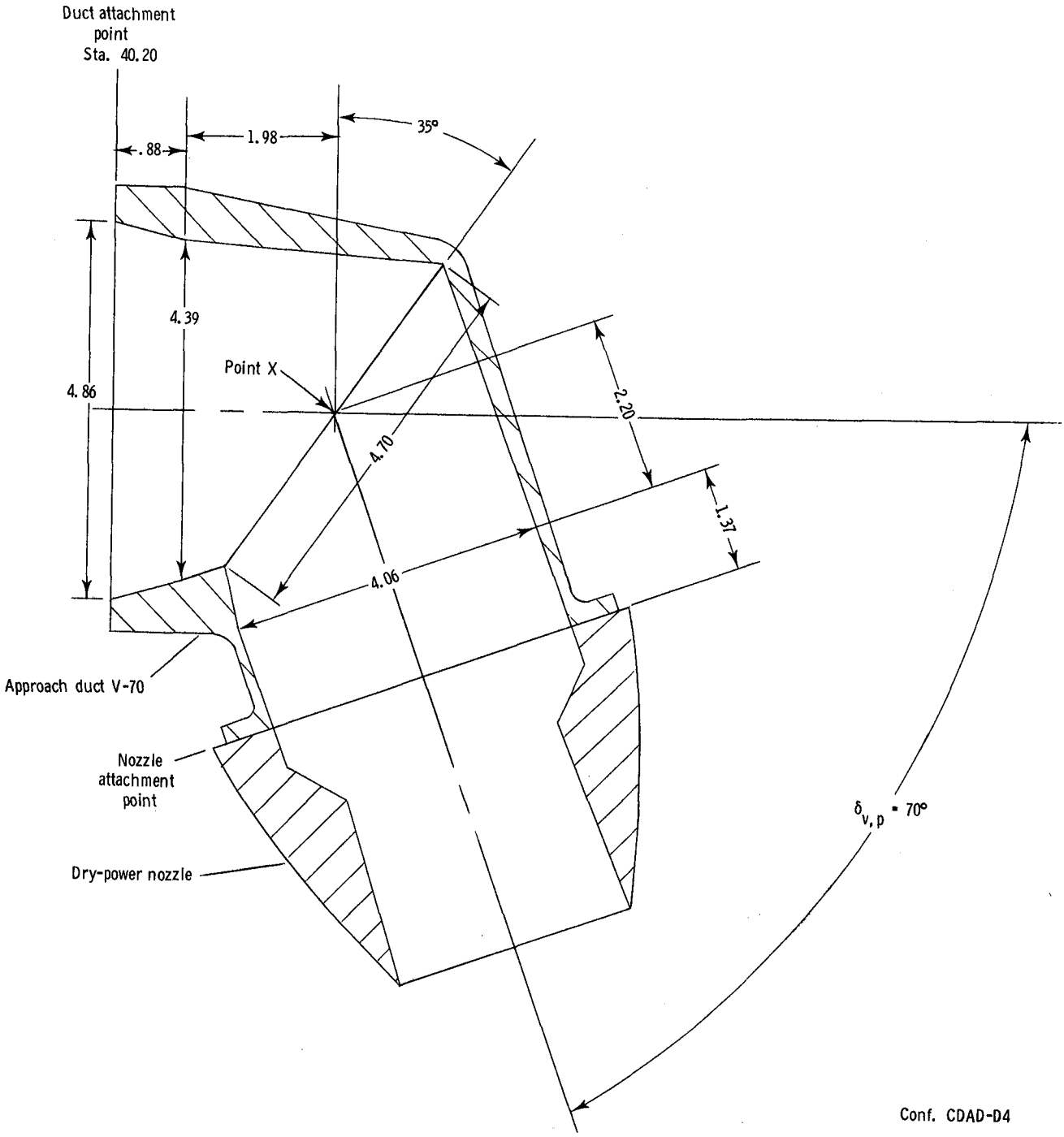

Figure 8.- Dry-power C-D nozzle with approach duct V-70 (counterrotating-duct geometry with $\delta_{v,p} = 70°$). See figure 2 for nozzle geometry details. Linear dimensions are in inches.

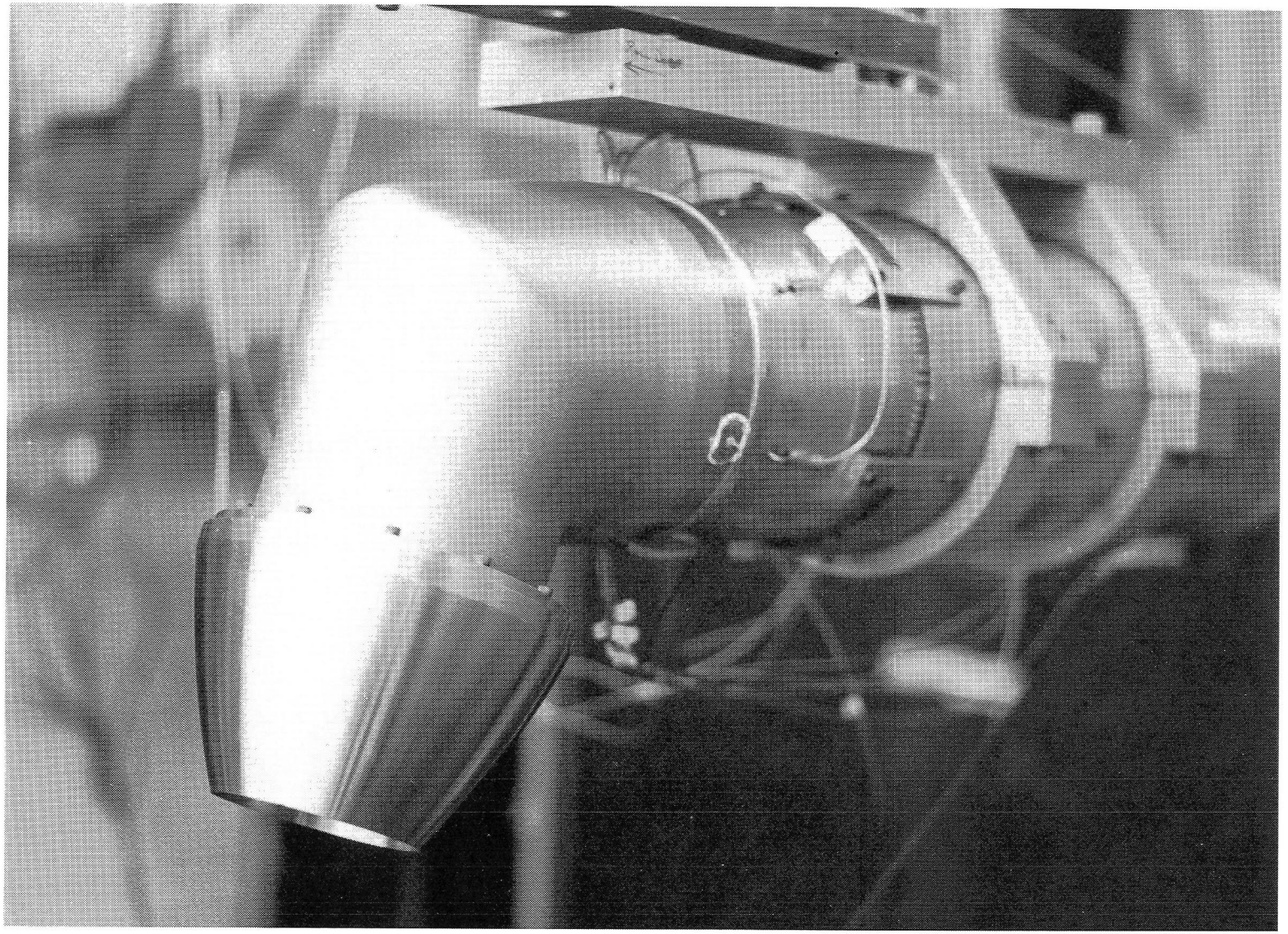

L-86-312

Figure 9.- Dry-power C-D nozzle configuration CDAD-D4 (with approach duct V-70) installed on single-engine propulsion simulation system.

Transition coordinates

ℓ	r	h
0.00	2.43	4.86
.25	2.22	4.72
.50	2.02	4.69
.75	1.80	4.62
1.00	1.60	4.55
1.25	1.39	4.49
1.50	1.18	4.44
1.75	0.97	4.40
2.00	.76	4.36
2.25	.55	4.34
2.50	.35	4.32
2.75	.14	4.31
2.92	.00	4.30

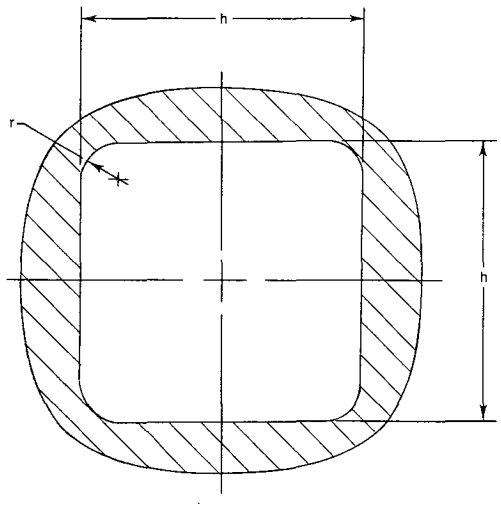

Section A-A

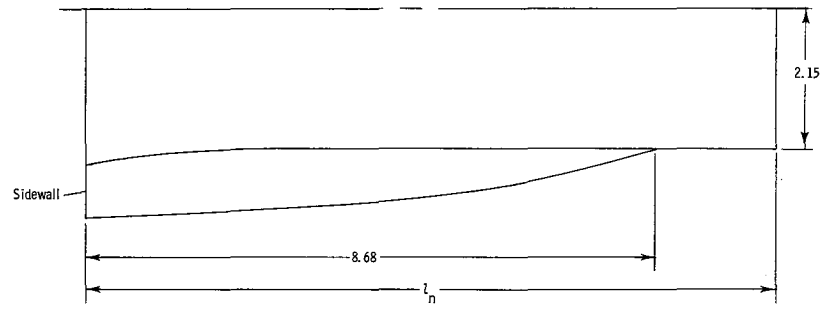

Top view

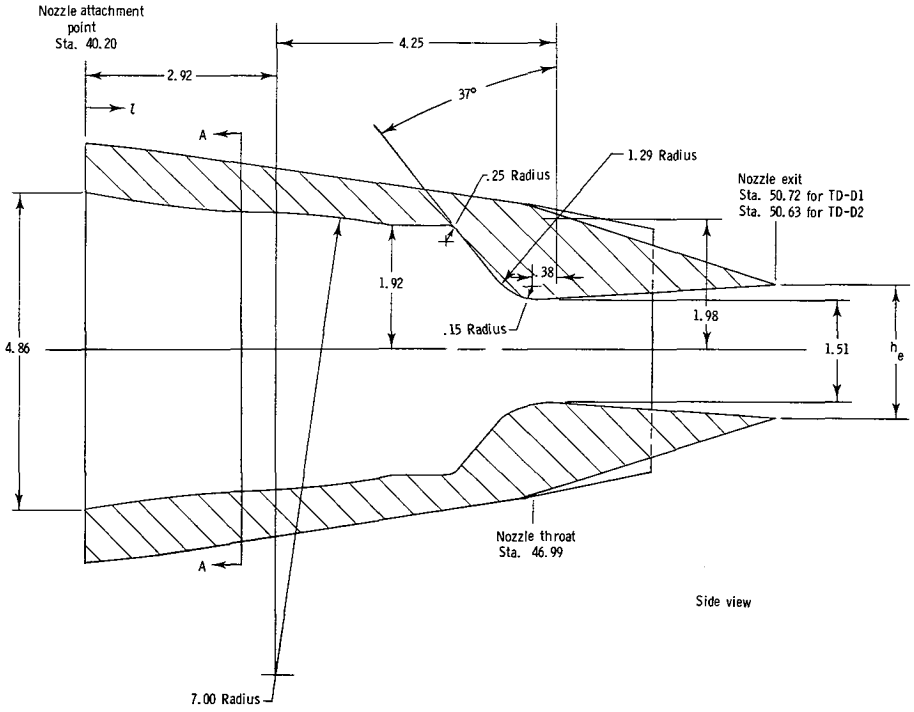

Side view

Configuration	A_e/A_t	A_t, in^2	h_e, in.	ℓ_n, in.	$(NPR)_{des}$	ε, deg
TD-D1	1.35	6.47	2.03	10.52	5.03	1.70
TD-D2	1.10	6.47	1.66	10.43	3.06	4.00

Figure 10.- Dry-power 2-D C-D nozzle configurations TD-D1 and TD-D2 ($\delta_{v,p} = 0°$). Linear dimensions are in inches.

Transition coordinates

ℓ	r	h
0.00	2.43	4.86
.25	2.22	4.72
.50	2.02	4.69
.75	1.80	4.62
1.00	1.60	4.55
1.25	1.39	4.49
1.50	1.18	4.44
1.75	0.97	4.40
2.00	.76	4.36
2.25	.55	4.34
2.50	.35	4.32
2.75	.14	4.31
2.92	.00	4.30

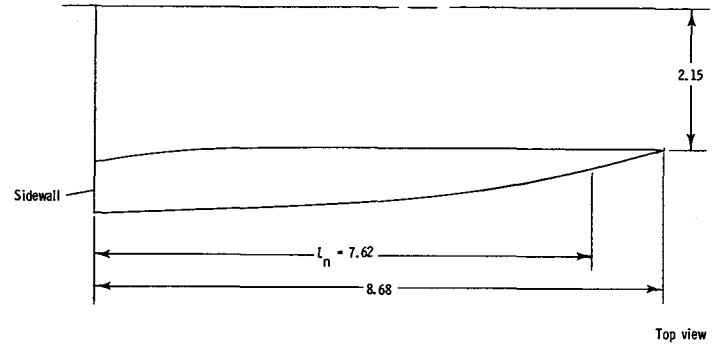

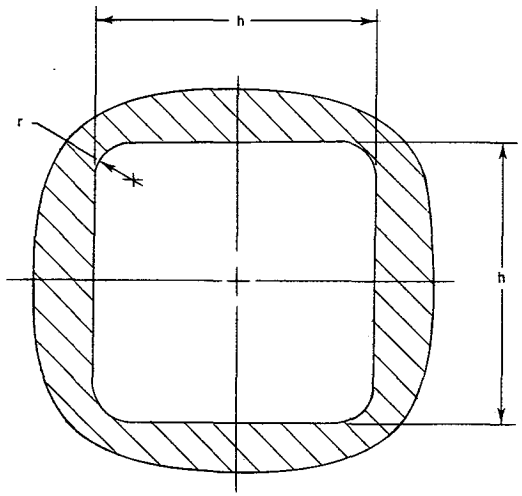

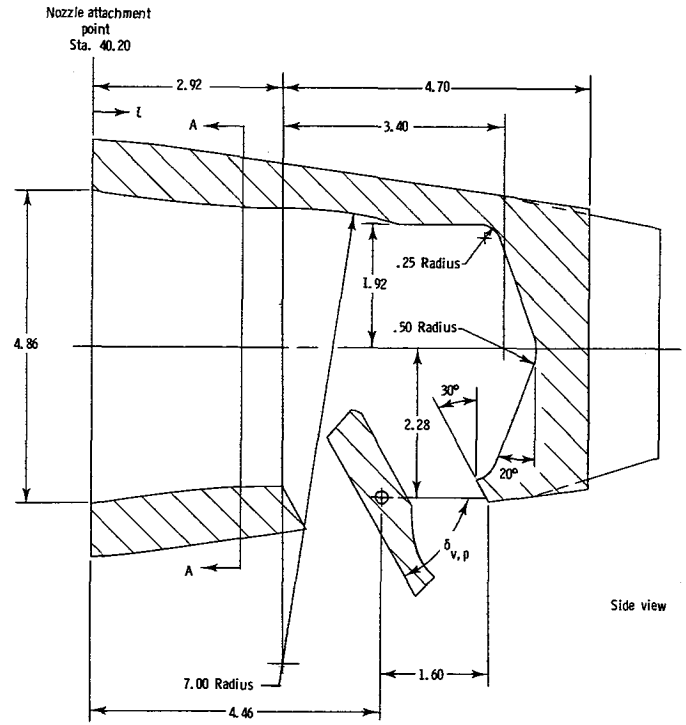

Configuration	A_t, in^2	$\delta_{v,p}$, deg
TD-D3	8.59	60.00
TD-D4	8.90	70.00

(a) Internal geometry for TD-D3 and TD-D4.

Figure 11.- Dry-power 2-D C-D pitch thrust-vectored nozzle configurations TD-D3 ($\delta_{v,p}$ = 60°) and TD-D4 ($\delta_{v,p}$ = 70°). Linear dimensions are in inches.

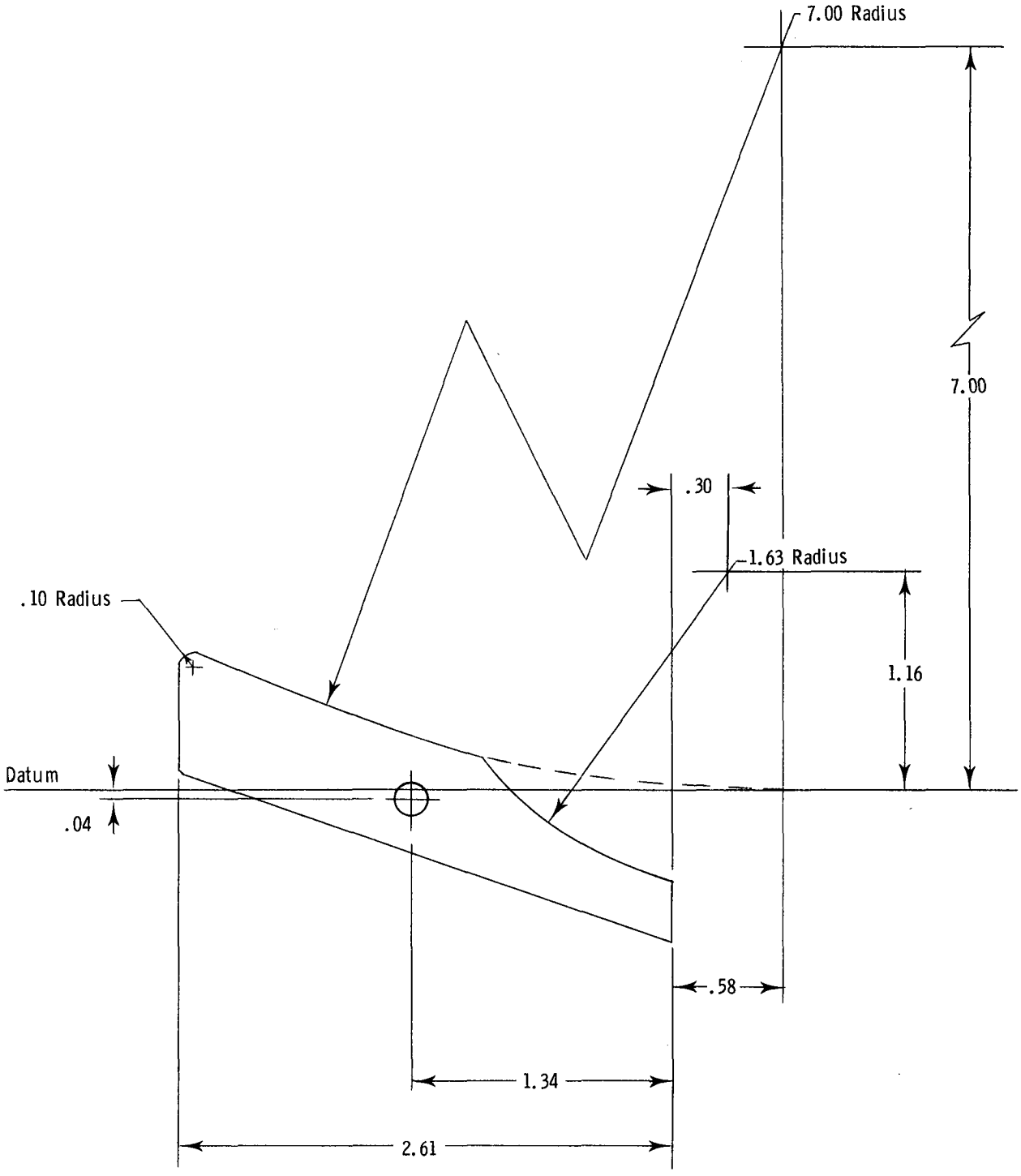

(b) Details of pitch-vectoring door.

Figure 11.- Concluded.

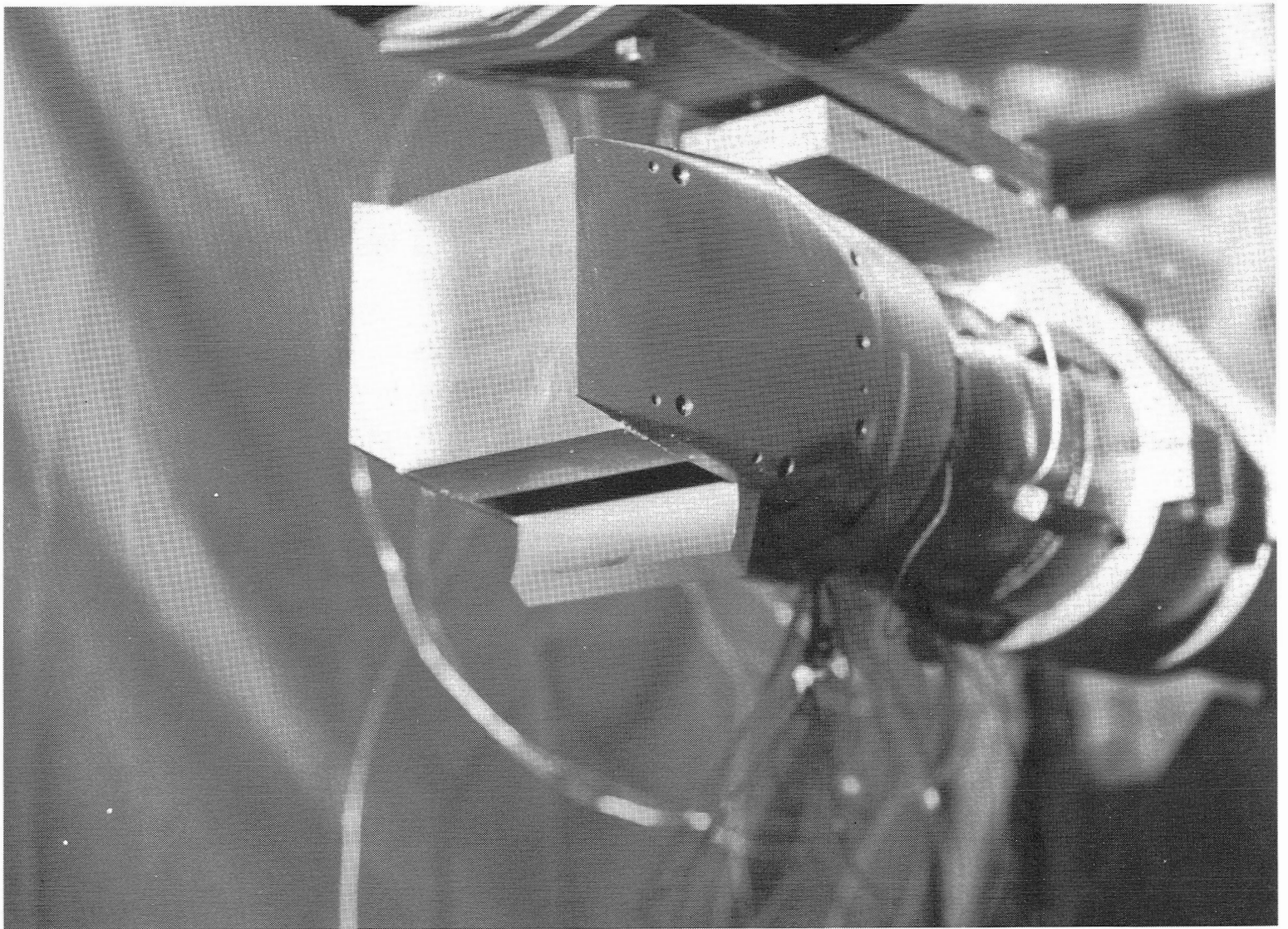

L-86-313

Figure 12.- Dry-power 2-D C-D nozzle configuration TD-D4 ($\delta_{v,p}$ = 70°) installed on single-engine propulsion simulation system.

Transition coordinates

ℓ	r	h
0.00	2.43	4.86
.25	2.22	4.72
.50	2.02	4.69
.75	1.80	4.62
1.00	1.60	4.55
1.25	1.39	4.49
1.50	1.18	4.44
1.75	0.97	4.40
2.00	.76	4.36
2.25	.55	4.34
2.50	.35	4.32
2.75	.14	4.31
2.92	.00	4.30

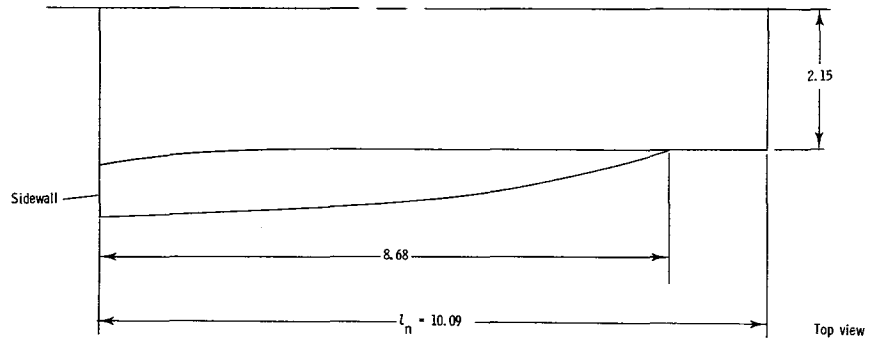

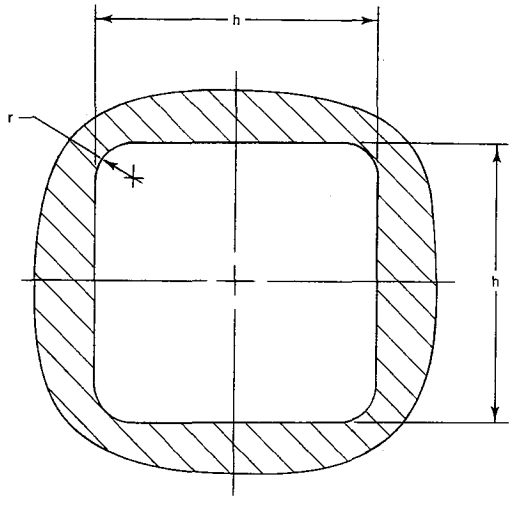

Section A-A

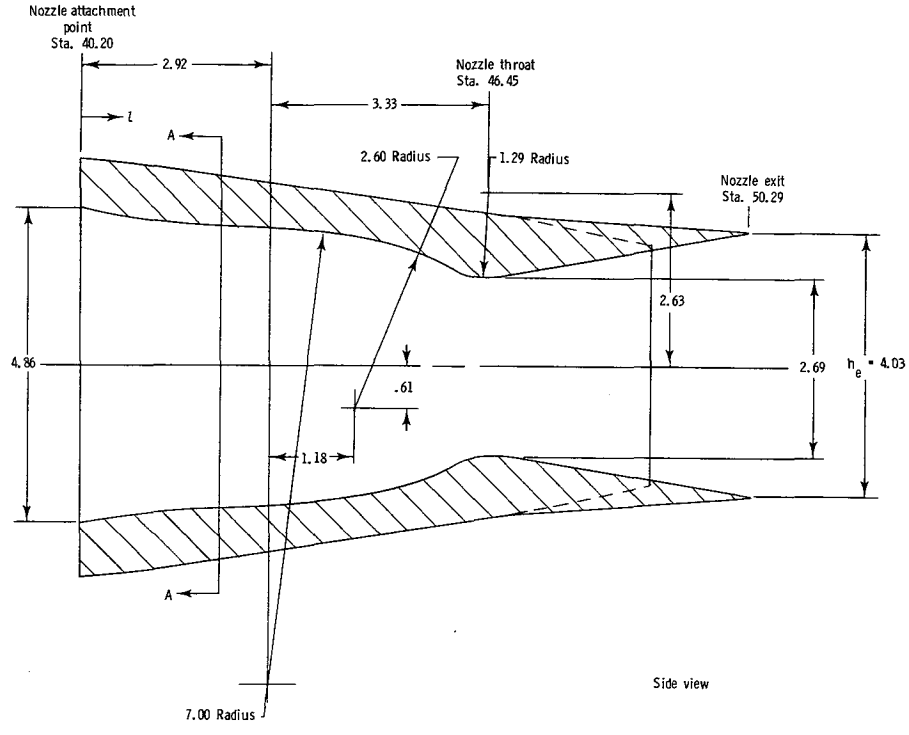

A_e/A_t = 1.50

A_t = 11.58 in^2

$(NPR)_{des}$ = 6.23

ε = 10.00 deg

Figure 13.- A/B-power 2-D C-D nozzle configuration TD-A1.
Linear dimensions are in inches.

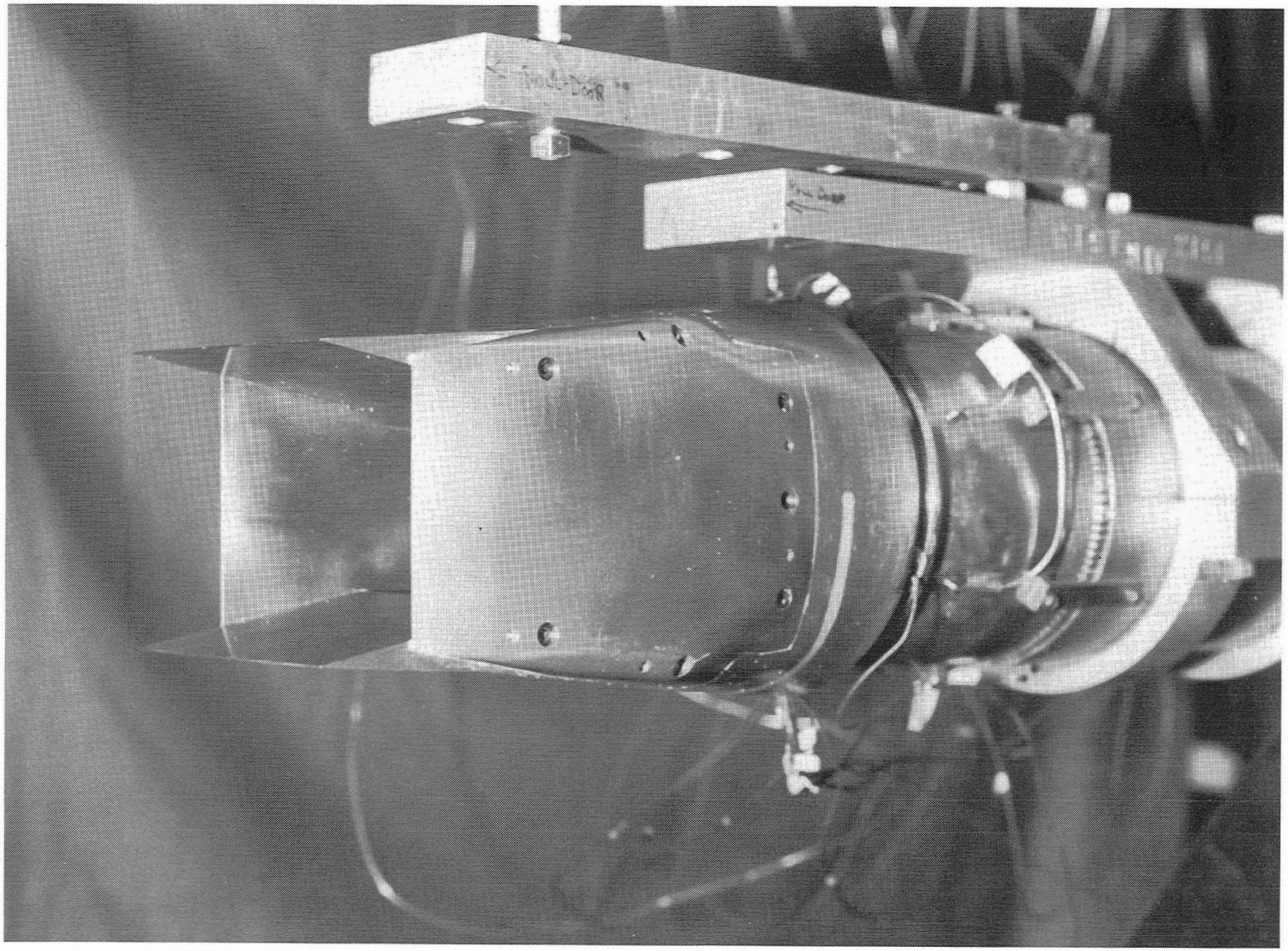

L-86-314

Figure 14.- A/B-power 2-D C-D nozzle configuration TD-A1 installed on single-engine propulsion simulation system.

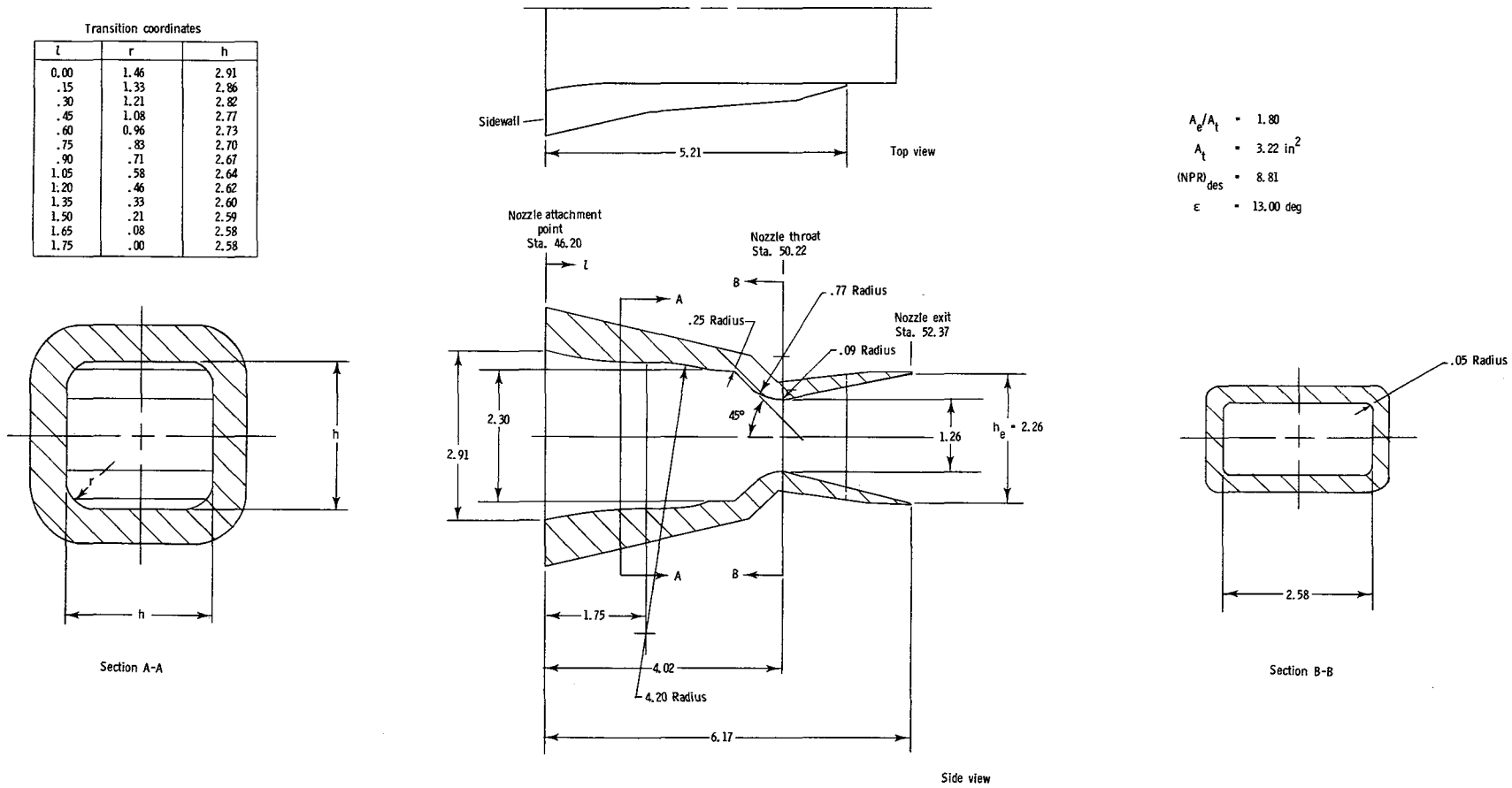

(a) Configuration TD-A2.

Figure 15.- A/B-power 2-D C-D nozzle configurations TD-A2, TD-A3, and TD-A4 with adaptor. Linear dimensions are in inches.

Transition coordinates

l	r	h
0.00	1.46	2.91
.15	1.33	2.86
.30	1.21	2.82
.45	1.08	2.77
.60	0.96	2.73
.75	.83	2.70
.90	.71	2.67
1.05	.58	2.64
1.20	.46	2.62
1.35	.33	2.60
1.50	.21	2.59
1.65	.08	2.58
1.75	.00	2.58

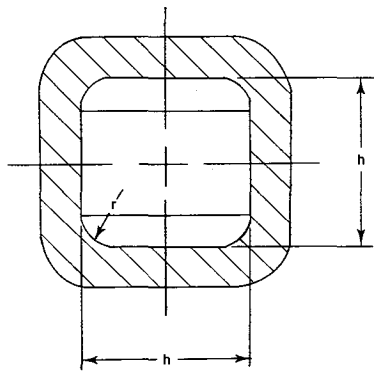

Section A-A

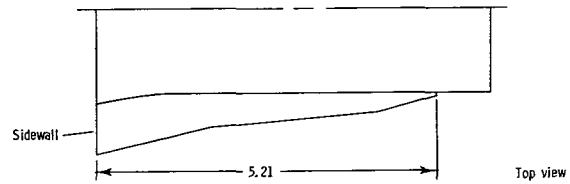

Top view

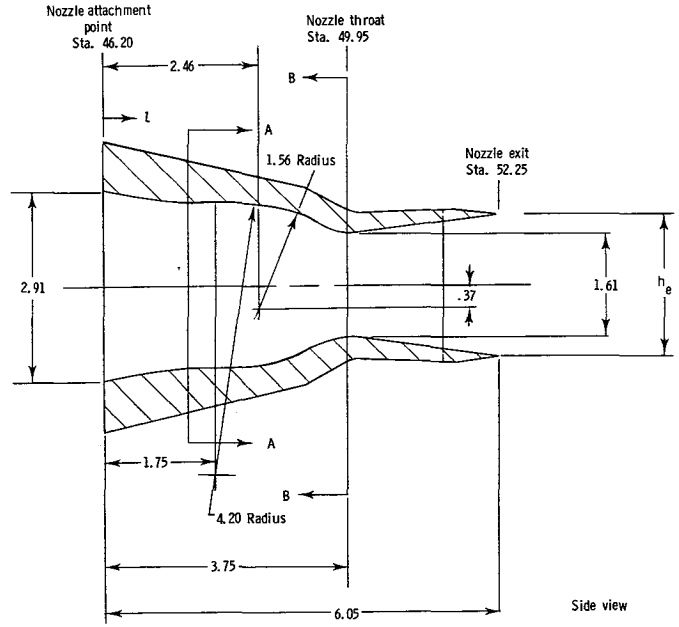

Side view

Configuration	A_e/A_t	A_t, in^2	h_e, in.	$(NPR)_{des}$	ε, deg
TD-A3	1.35	4.16	2.18	5.03	7.00
TD-A4	1.50	4.17	2.42	6.23	10.00

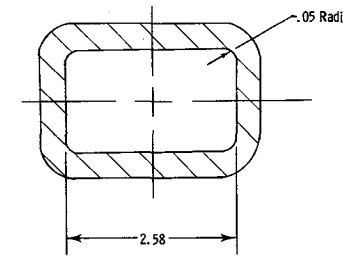

Section B-B

(b) Configurations TD-A3 and TD-A4.

Figure 15.- Continued.

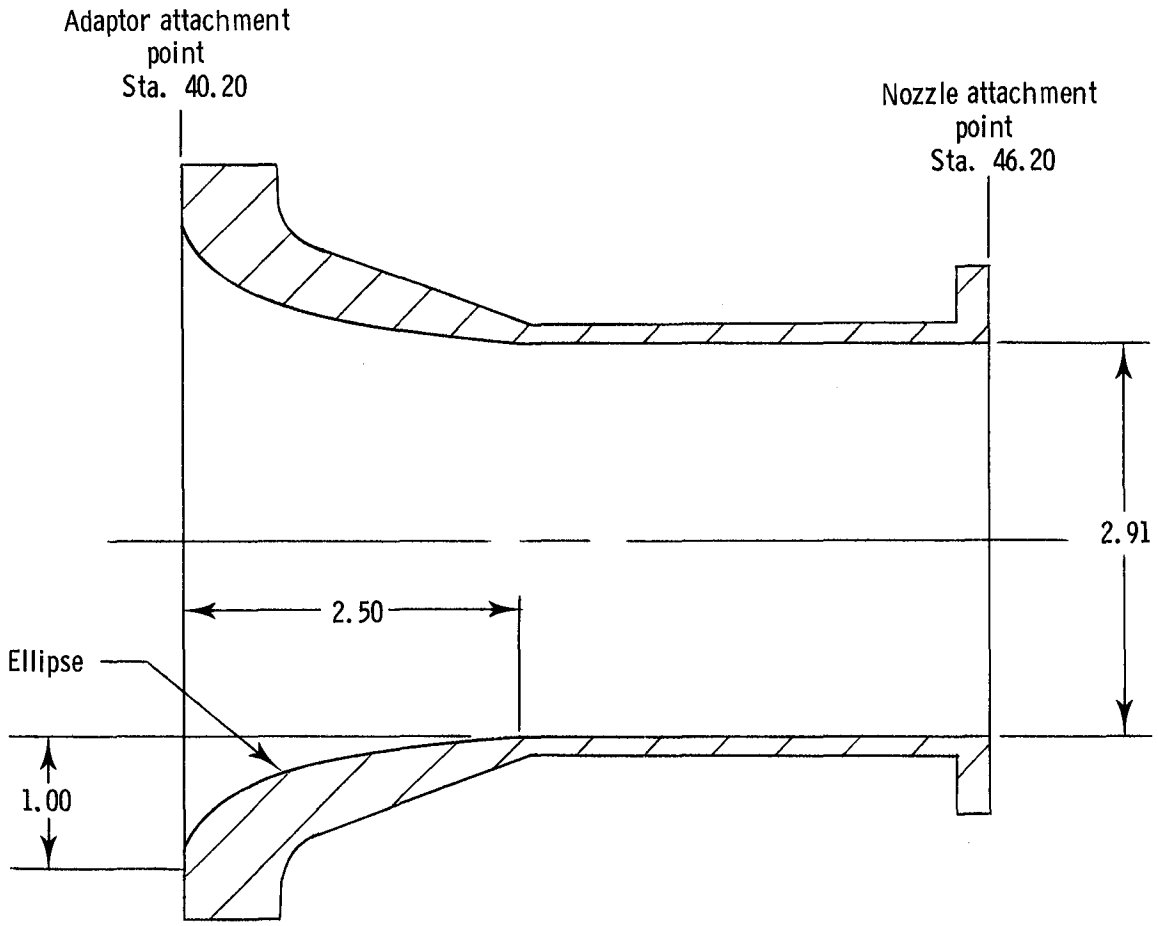

(c) Nozzle adaptor for TD-A2, TD-A3, and TD-A4.

Figure 15.- Concluded.

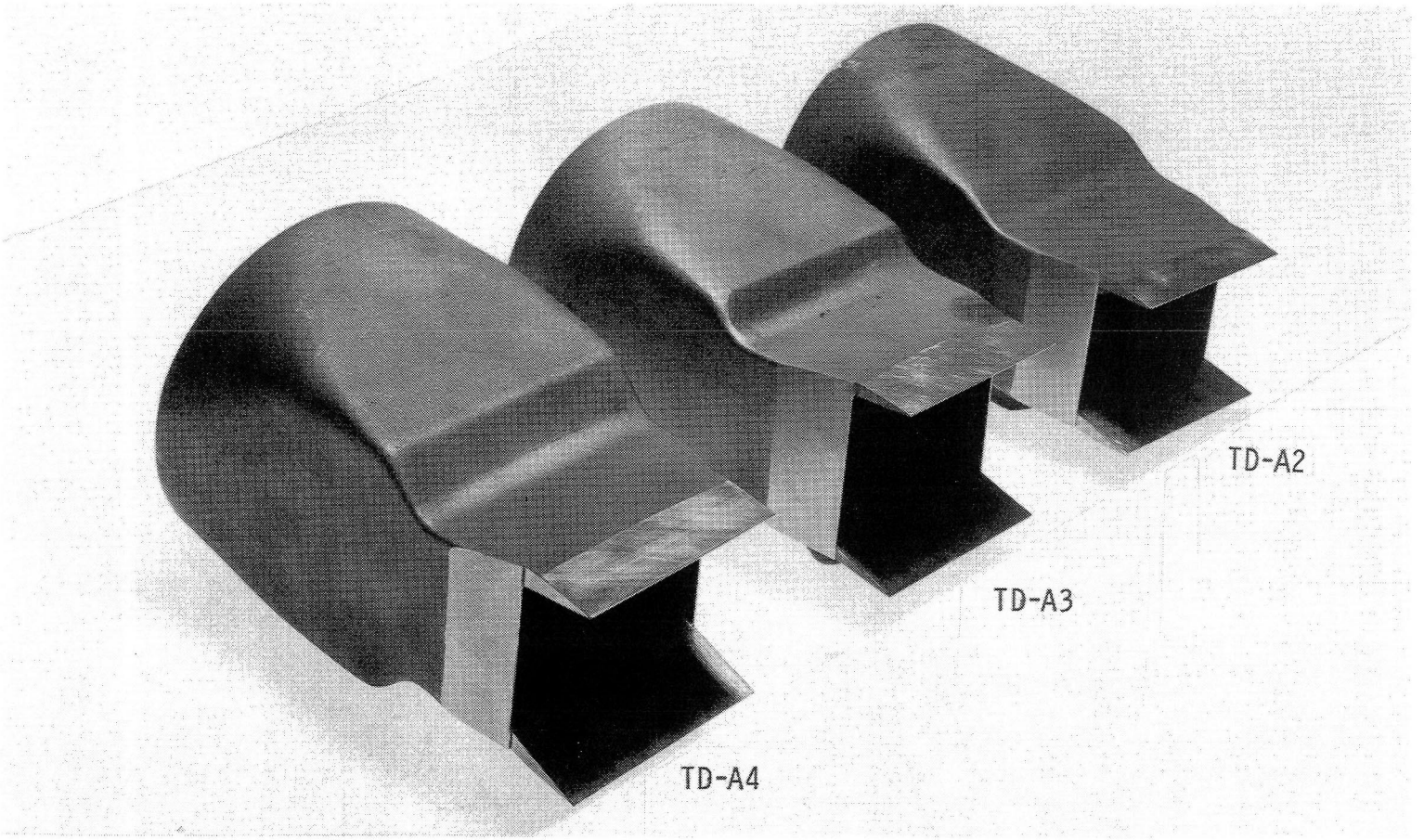

L-86-315

Figure 16.- A/B-power 2-D C-D nozzle configurations TD-A2, TD-A3, and TD-A4 (adaptor not shown).

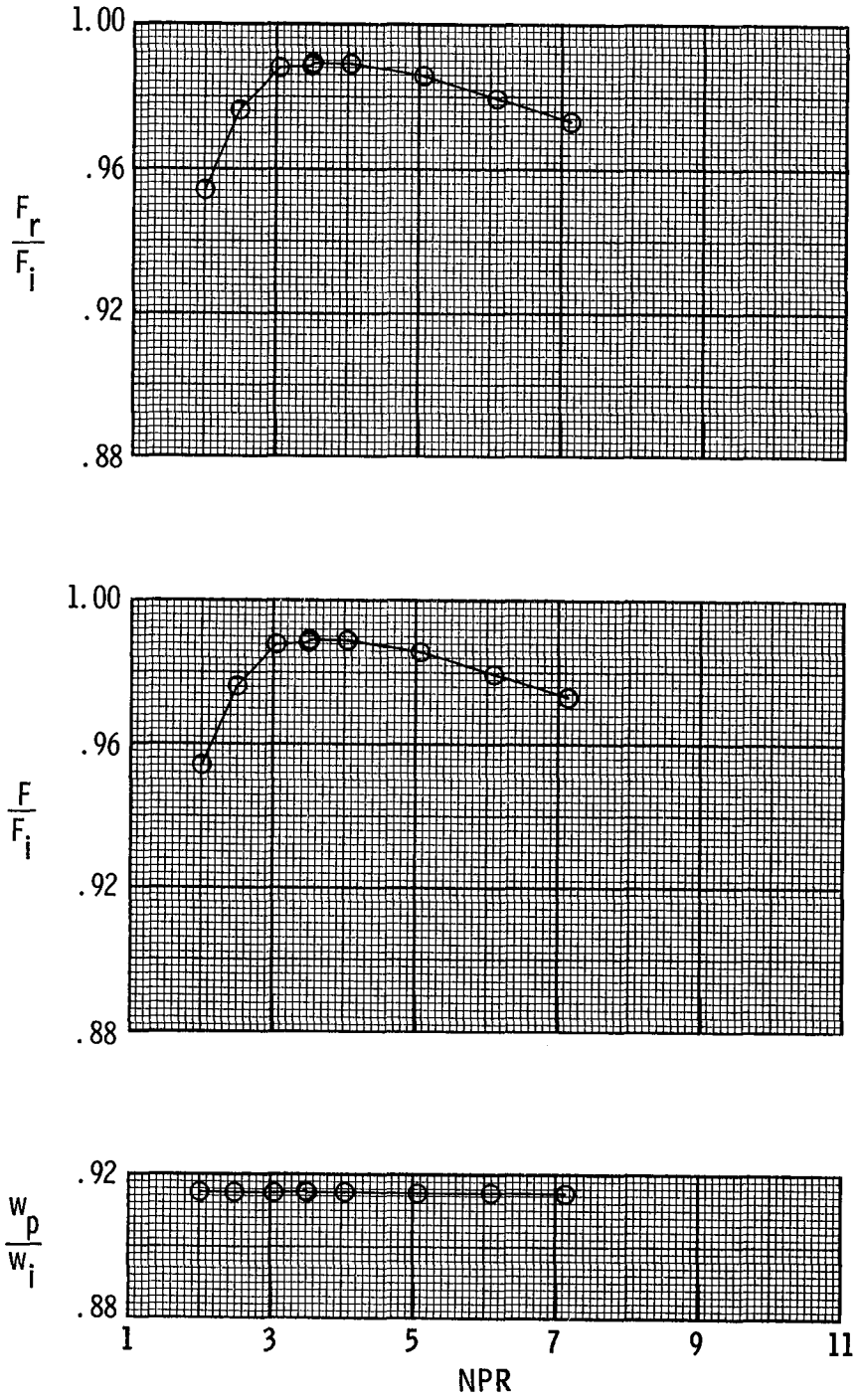

(a) Configuration CDAD-D1 (dry power, $\delta_{v,p} = 0°$).

Figure 17.- Variation of nozzle discharge coefficient, thrust ratio, and resultant thrust ratio with NPR for C-D nozzles with approach duct U-0.

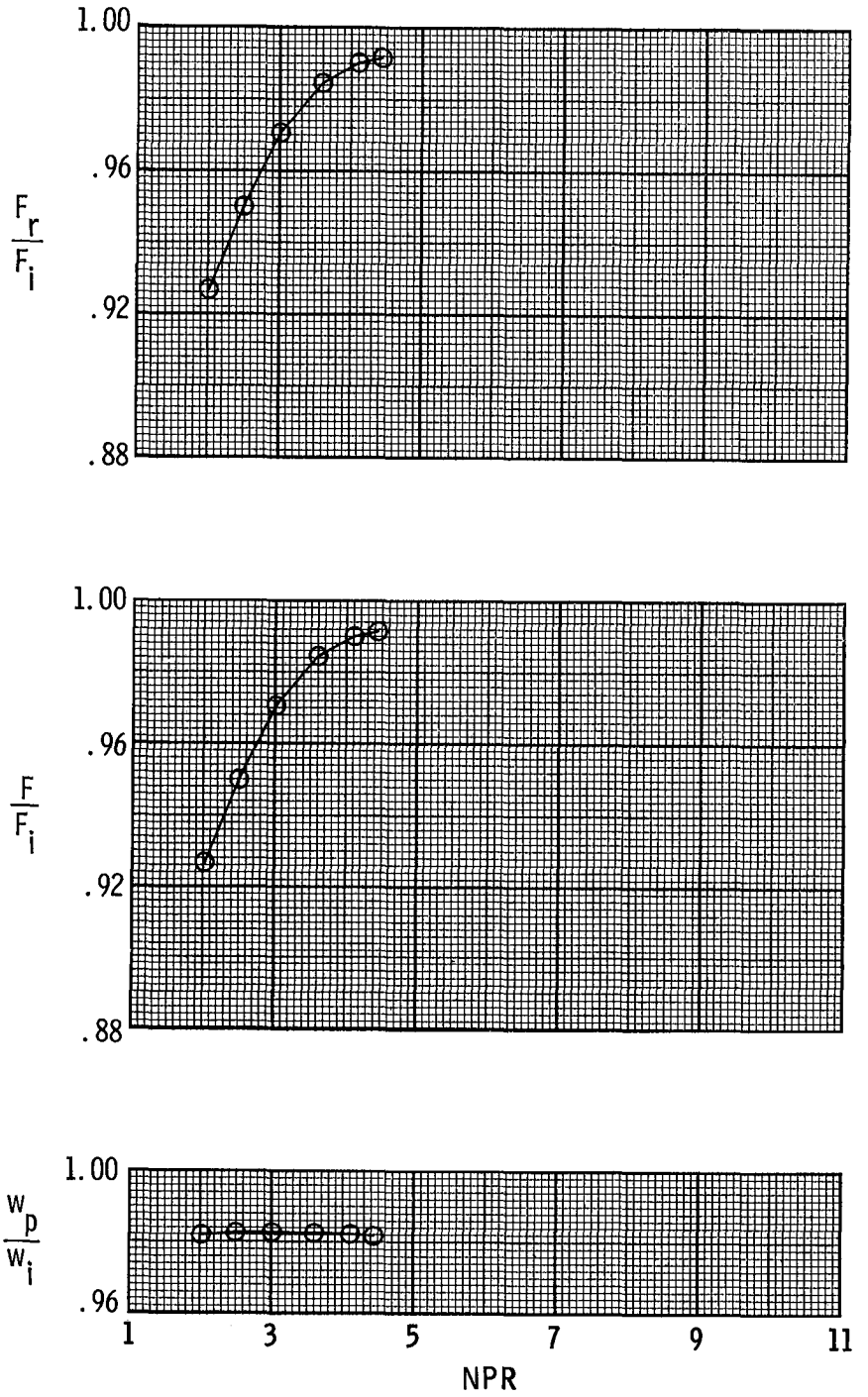

(b) Configuration CDAD-A1 (A/B power, $\delta_{v,p} = 0°$).

Figure 17.- Concluded.

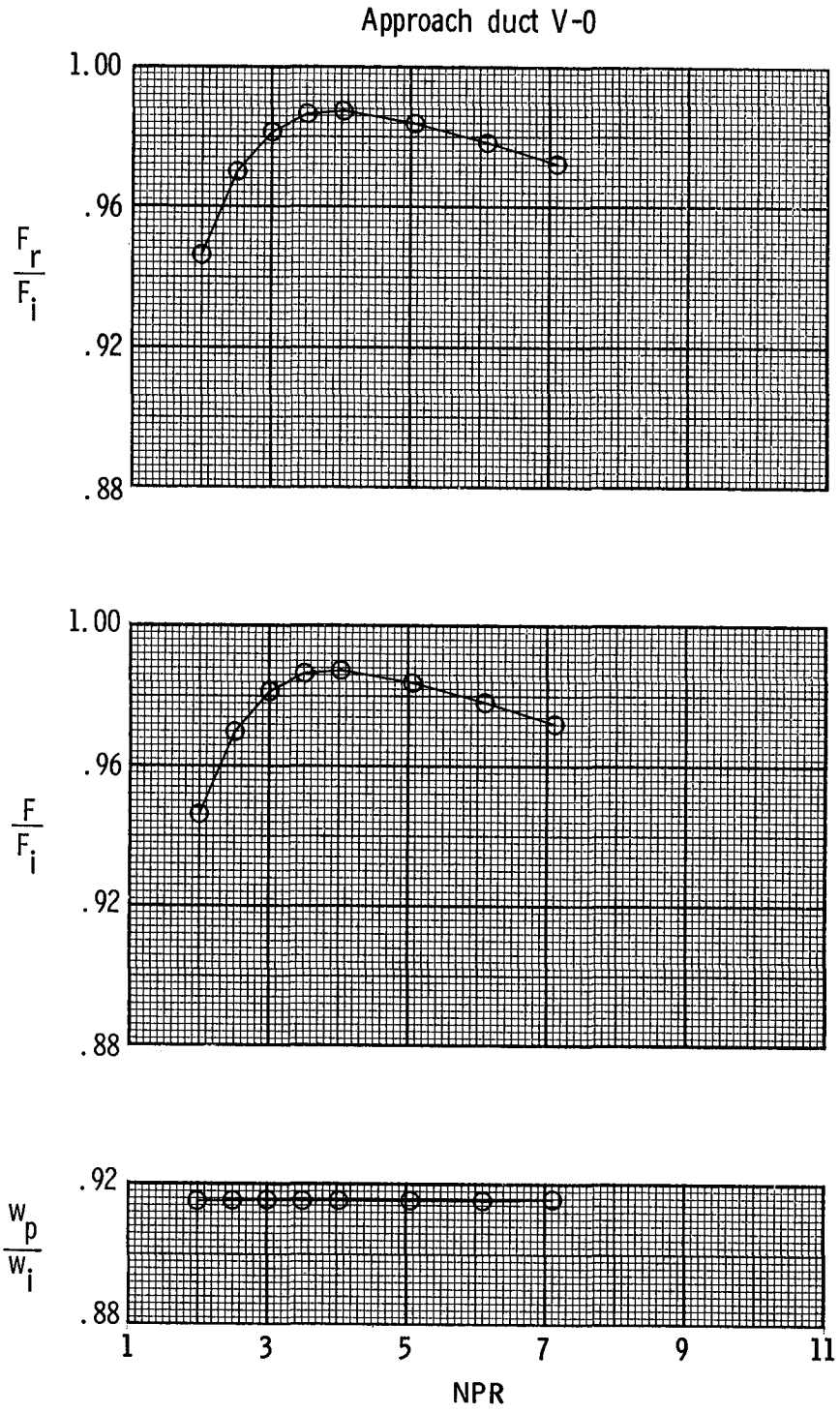

(a) Configuration CDAD-D2 (dry power, $\delta_{v,p} = 0°$).

Figure 18.- Variation of nozzle discharge coefficient, thrust ratio, and resultant thrust ratio with NPR for C-D nozzles with approach duct V.

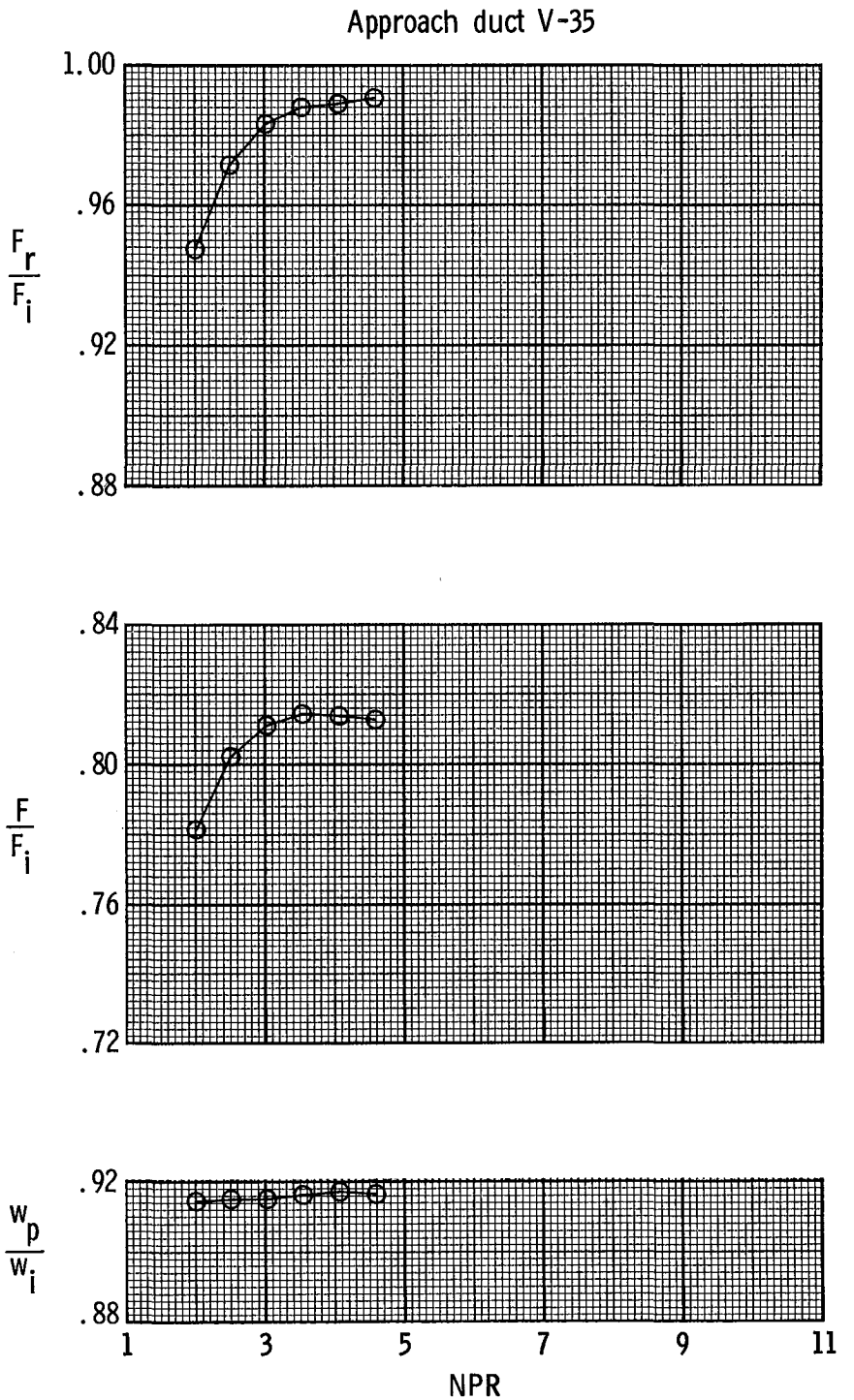

(b) Configuration CDAD-D3 (dry power, $\delta_{v,p} = 35°$).

Figure 18.- Continued.

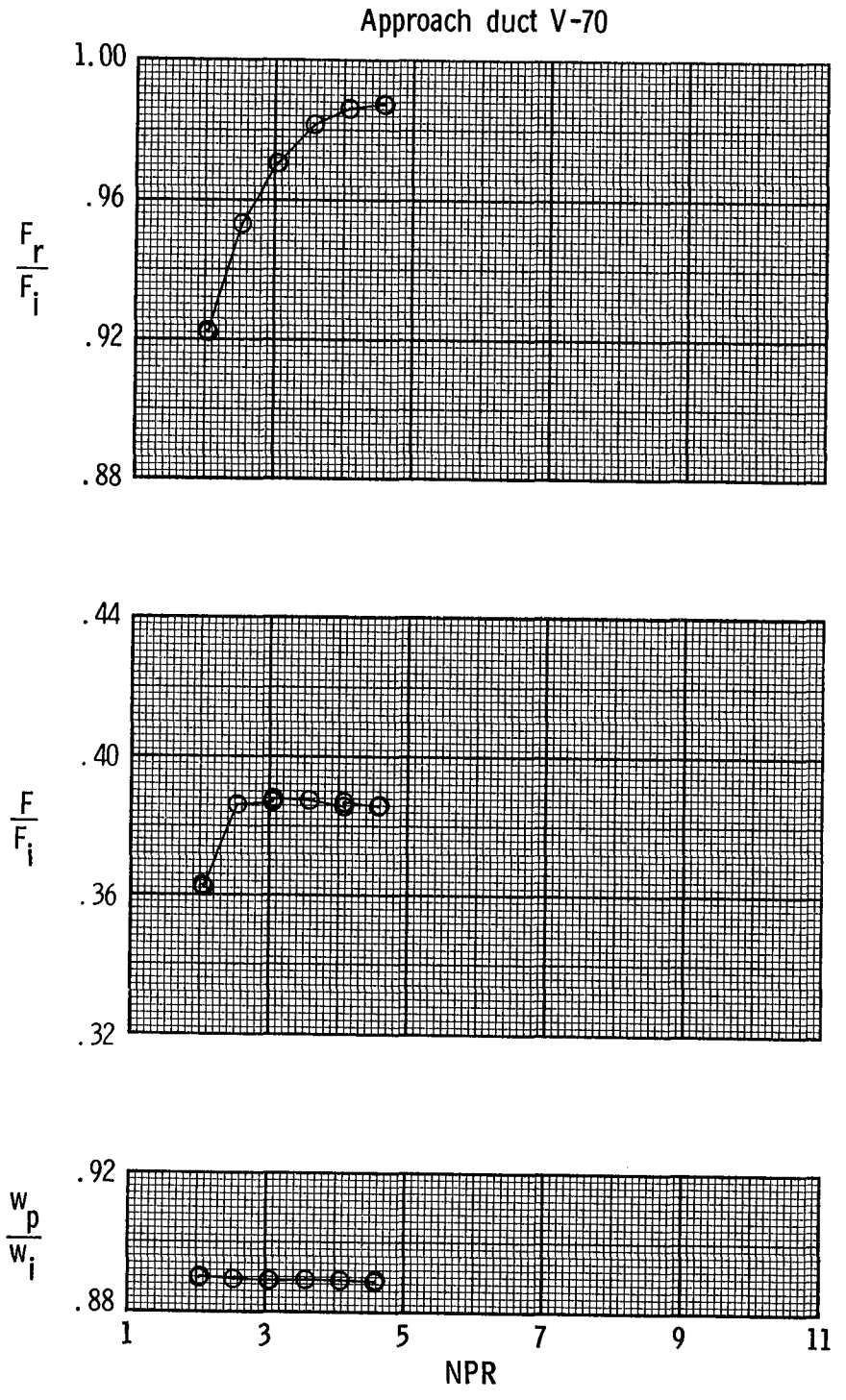

(c) Configuration CDAD-D4 (dry power, $\delta_{v,p} = 70°$).

Figure 18.- Continued.

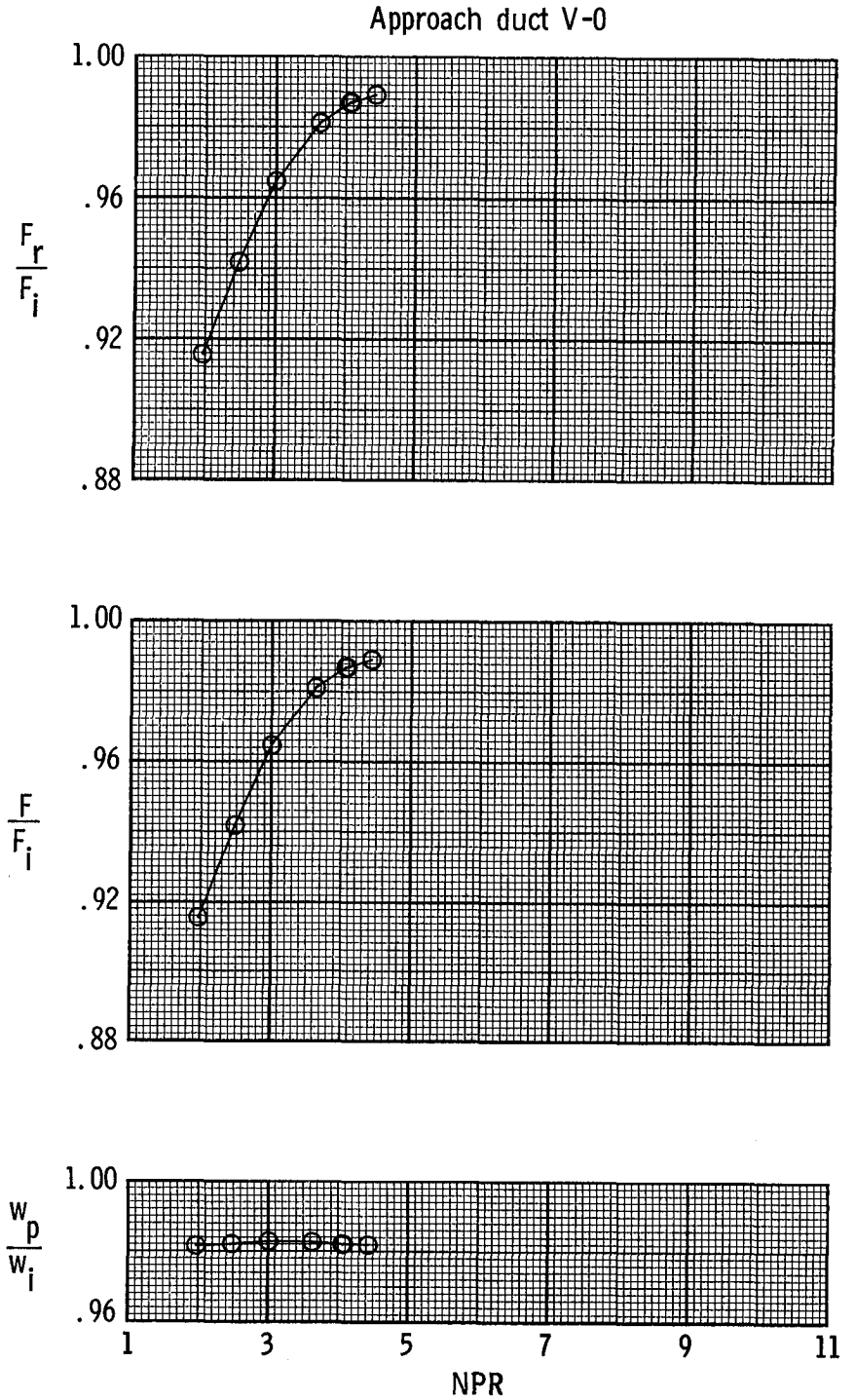

(d) Configuration CDAD-A2 (A/B power, $\delta_{v,p} = 0°$).

Figure 18.- Concluded.

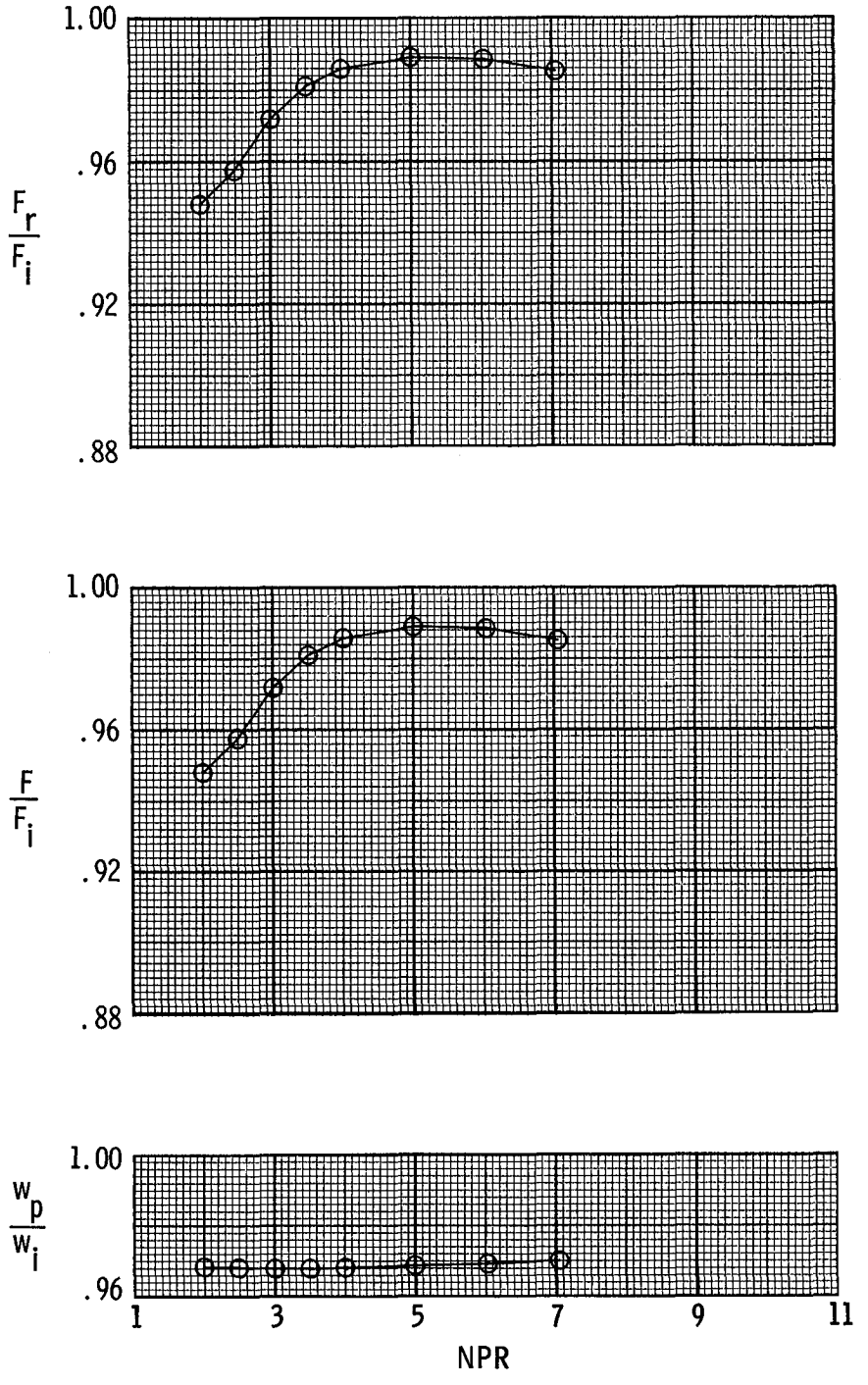

(a) Configuration TD-D1 ($\delta_{v,p} = 0°$); $A_e/A_t = 1.35$.

Figure 19.- Variation of nozzle discharge coefficient, thrust ratio, and resultant thrust ratio with NPR for dry-power 2-D C-D nozzle configurations.

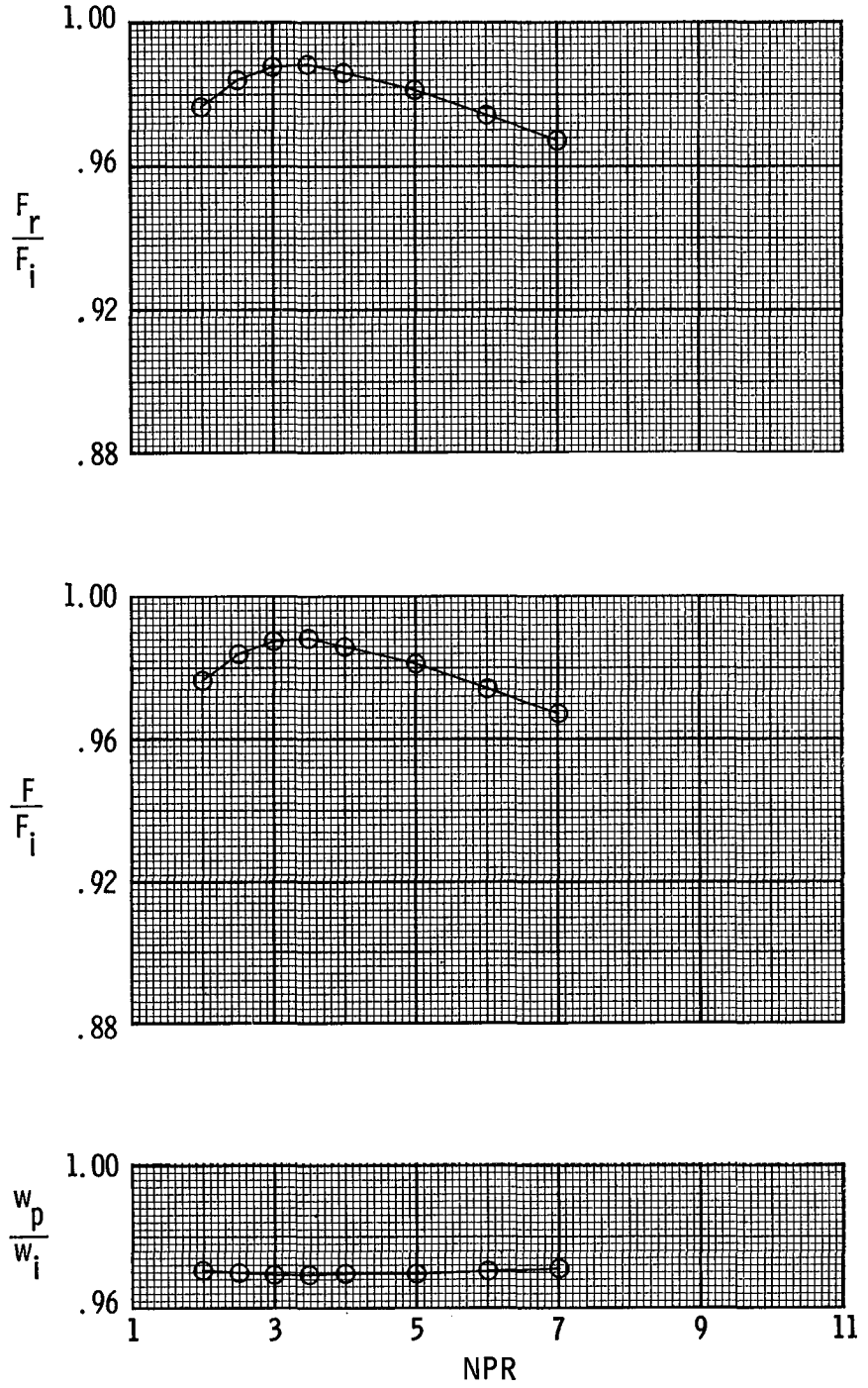

(b) Configuration TD-D2 ($\delta_{v,p}$ = 0°); A_e/A_t = 1.10.

Figure 19.- Continued.

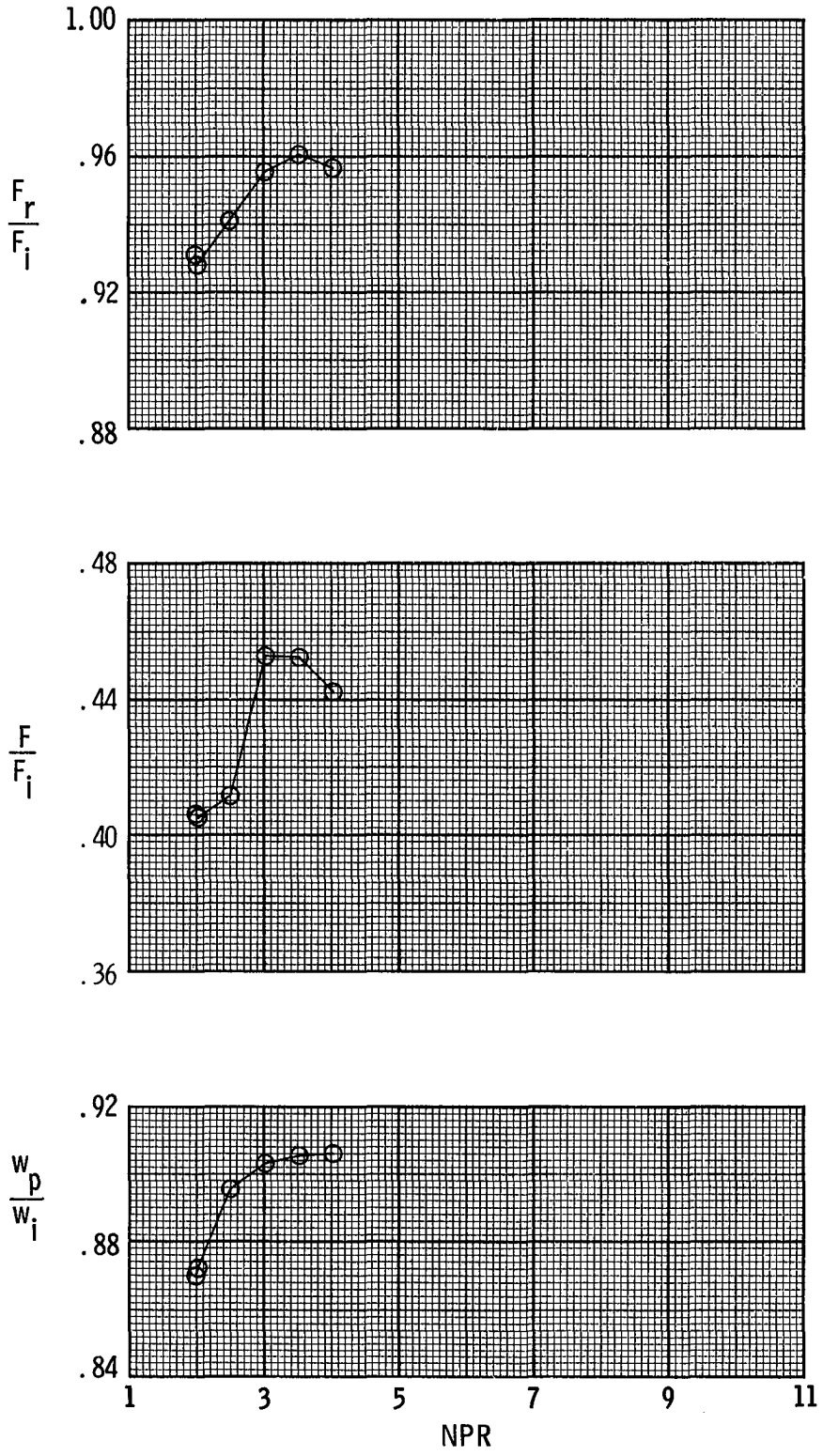

(c) Configuration TD-D3 ($\delta_{v,p}$ = 60°).

Figure 19.- Continued.

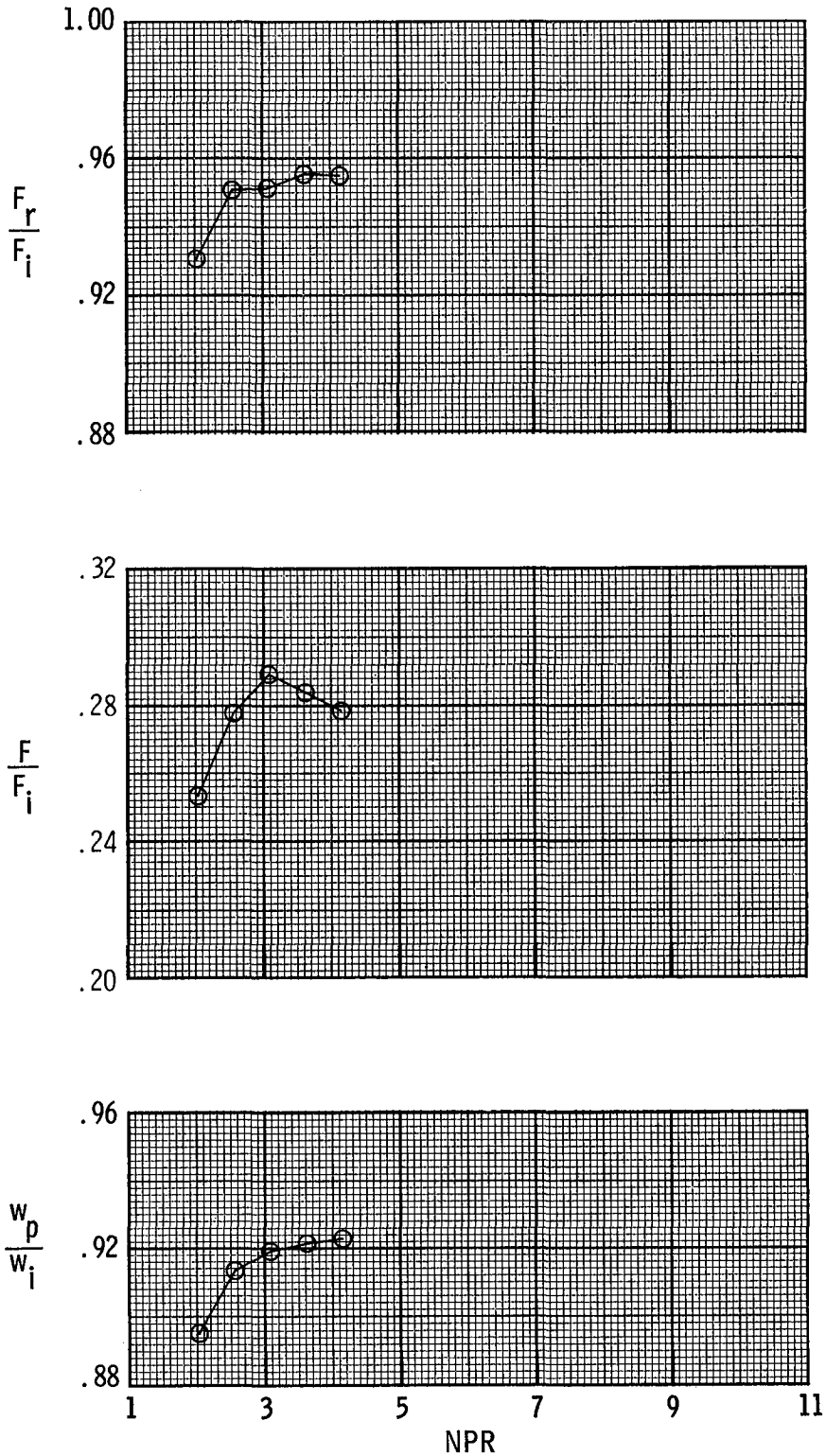

(d) Configuration TD-D4 ($\delta_{v,p}$ = 70°).

Figure 19.- Concluded.

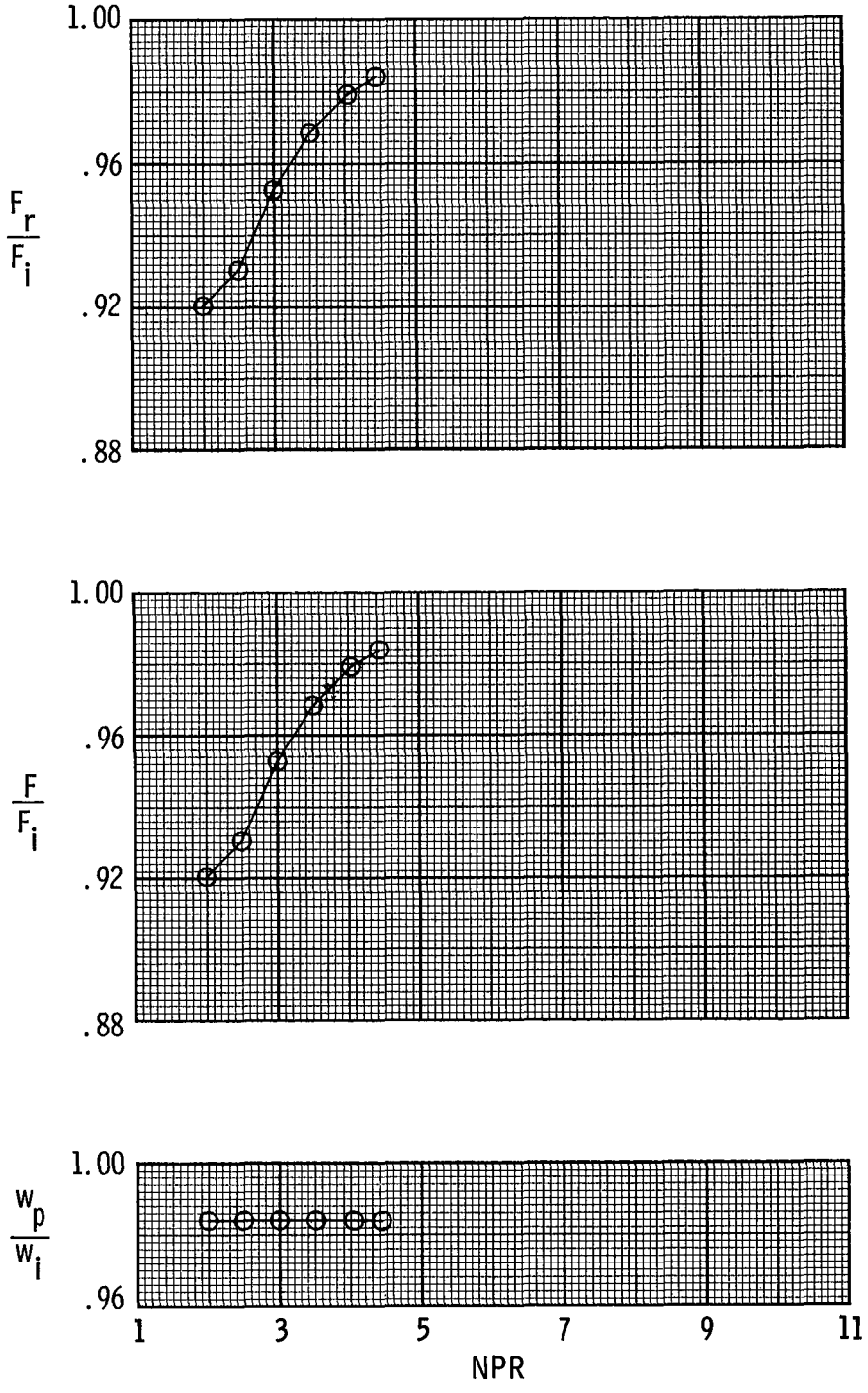

(a) Configuration TD-A1 ($\delta_{v,p} = 0°$); $A_e/A_t = 1.50$.

Figure 20.- Variation of nozzle discharge coefficient, thrust ratio, and resultant thrust ratio with NPR for A/B-power 2-D C-D nozzle configurations.

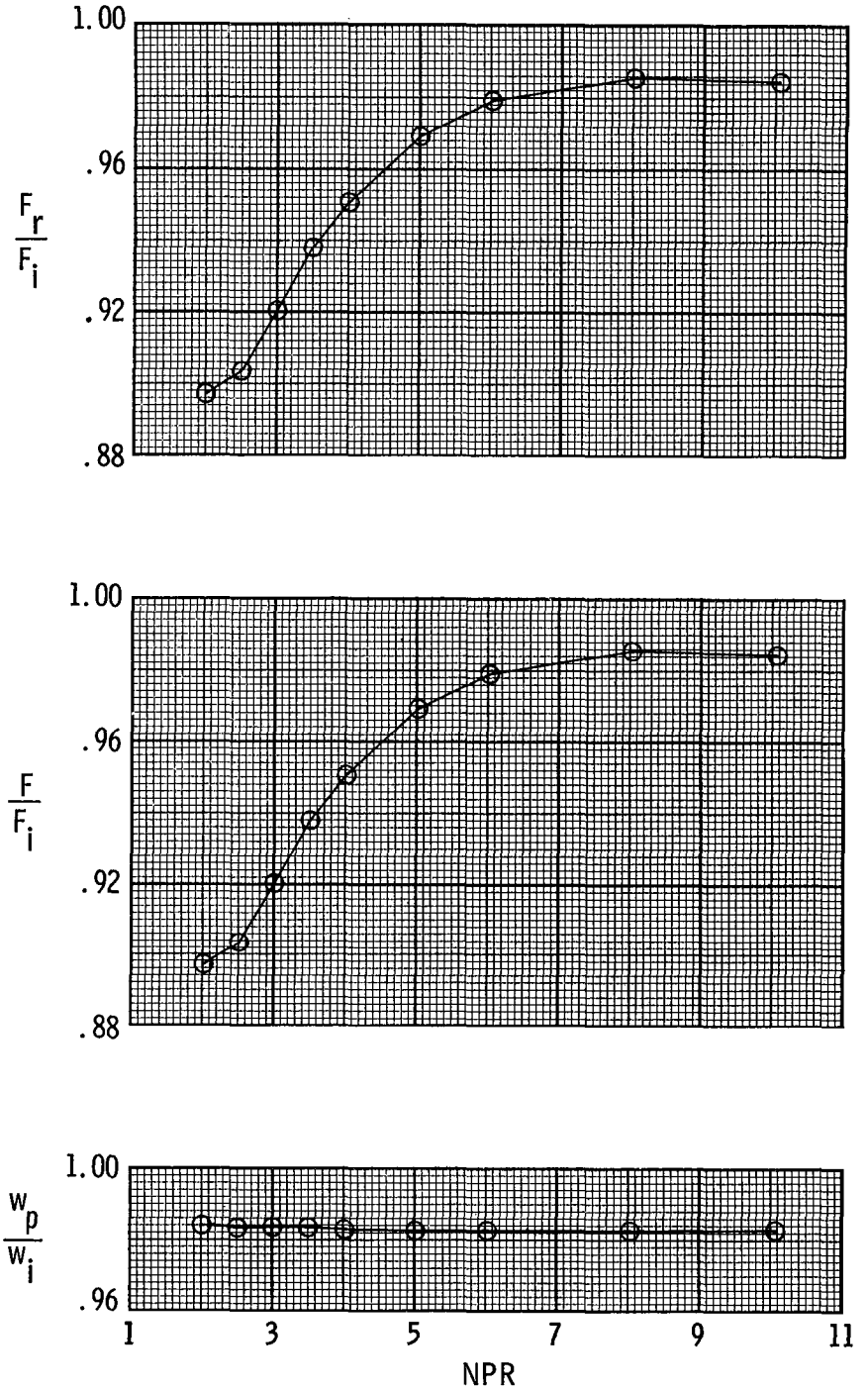

(b) Configuration TD-A2 ($\delta_{v,p} = 0°$); $A_e/A_t = 1.80$.

Figure 20.- Continued.

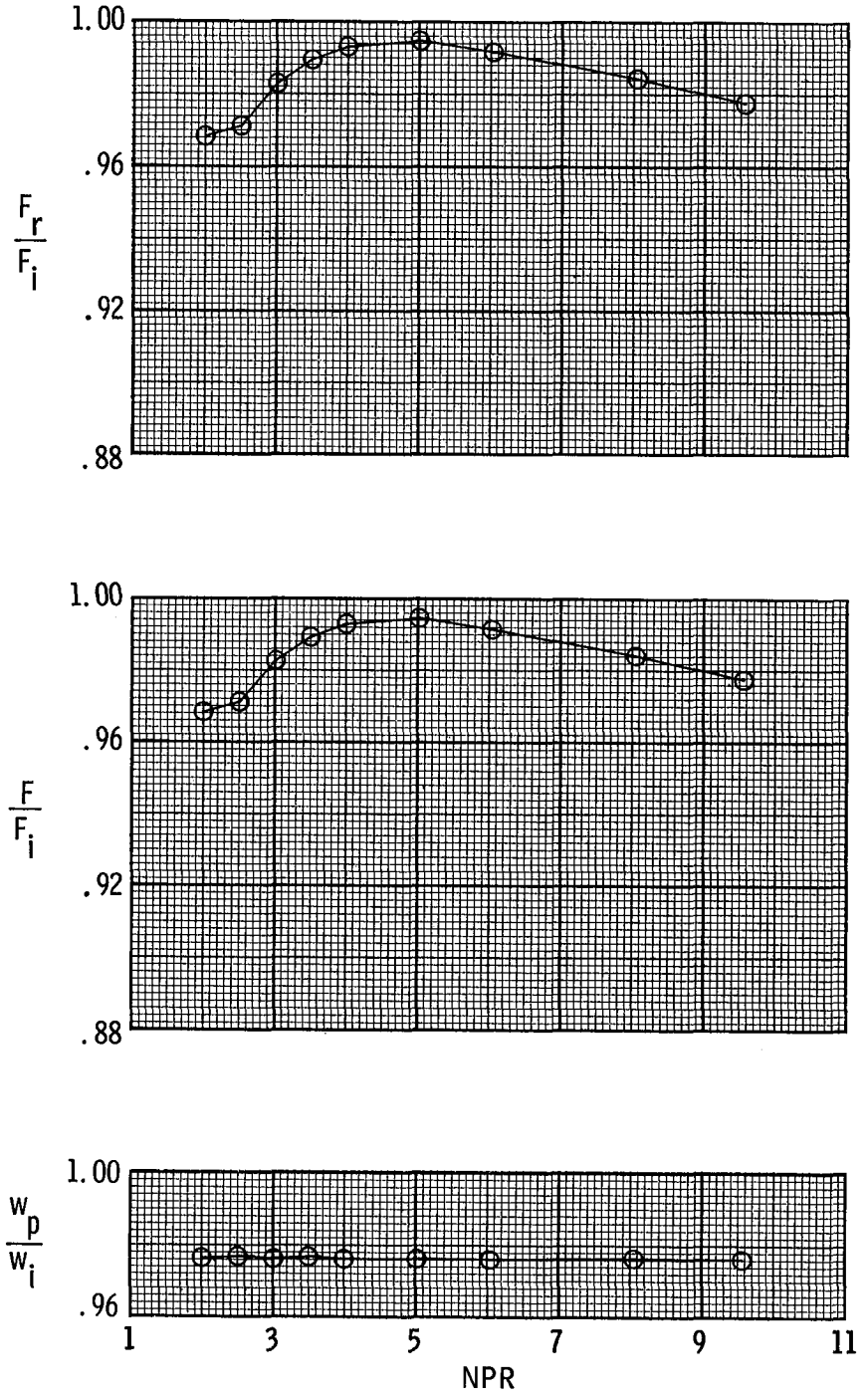

(c) Configuration TD-A3 ($\delta_{v,p}$ = 0°); A_e/A_t = 1.35.

Figure 20.- Continued.

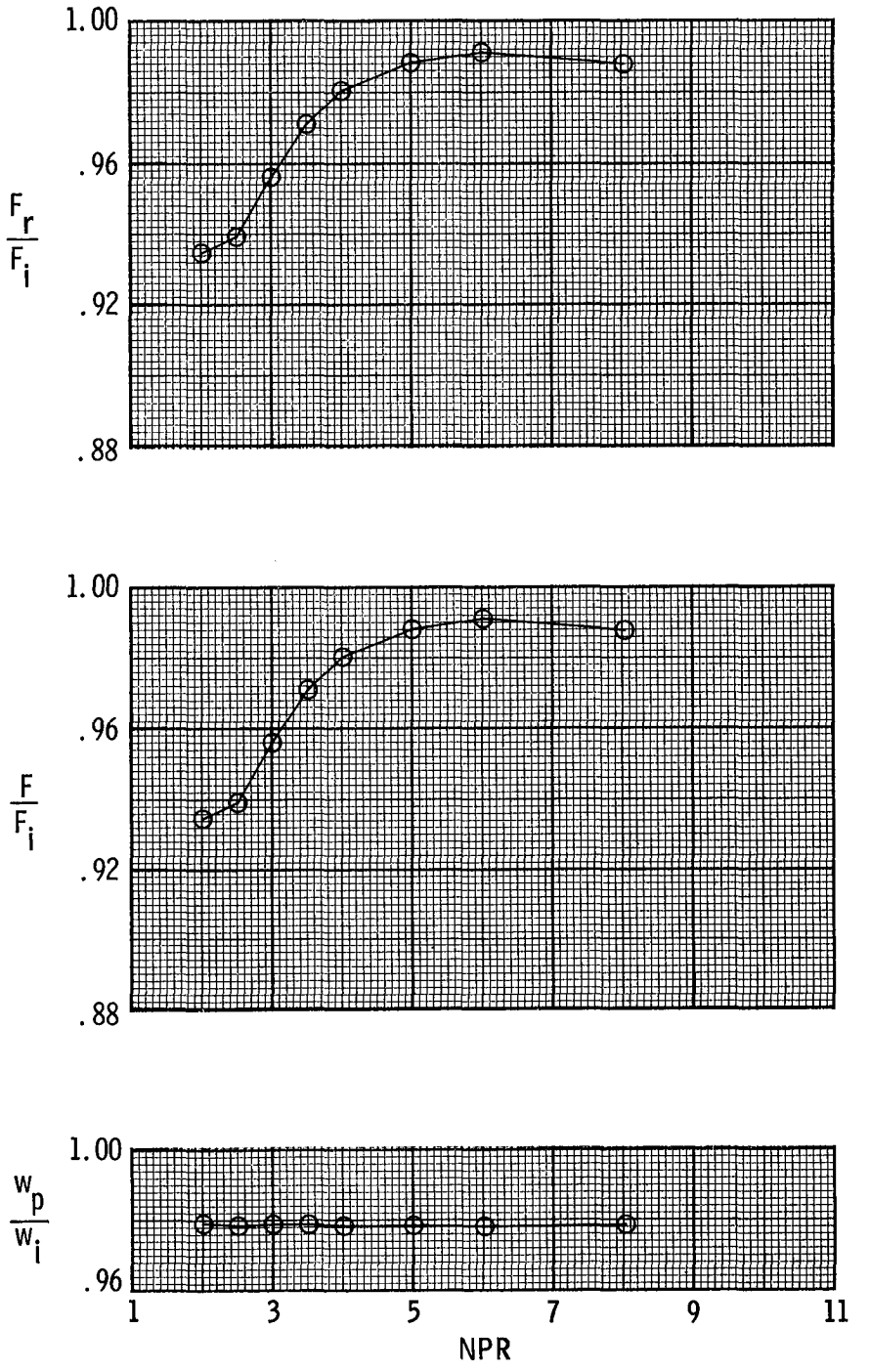

(d) Configuration TD-A4 ($\delta_{v,p}$ = 0°); A_e/A_t = 1.50.

Figure 20.- Concluded.

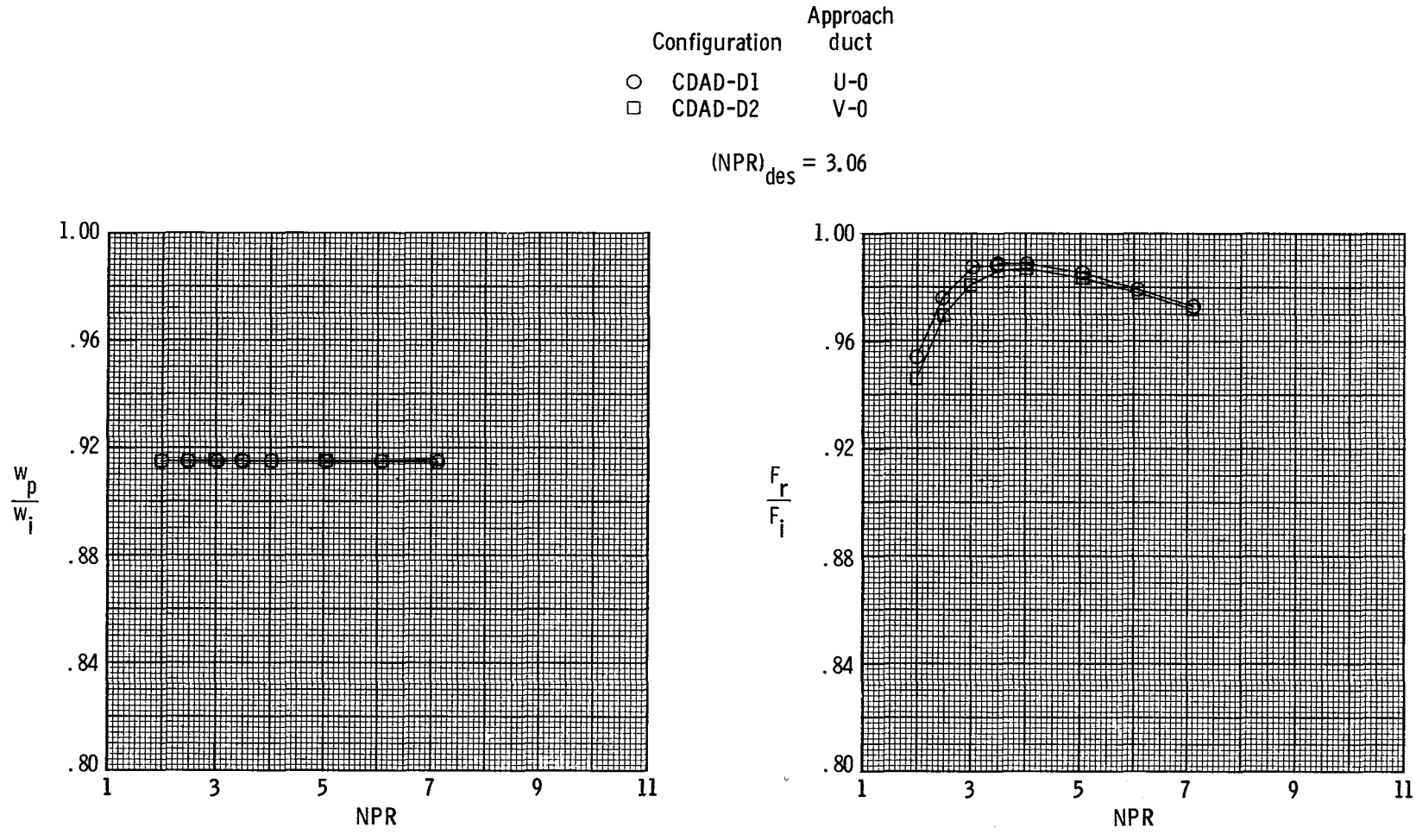

Figure 21.- Effect of approach-duct geometry on nozzle discharge coefficient and resultant thrust ratio for dry-power CDAD configurations. $\delta_{v,p} = 0°$.

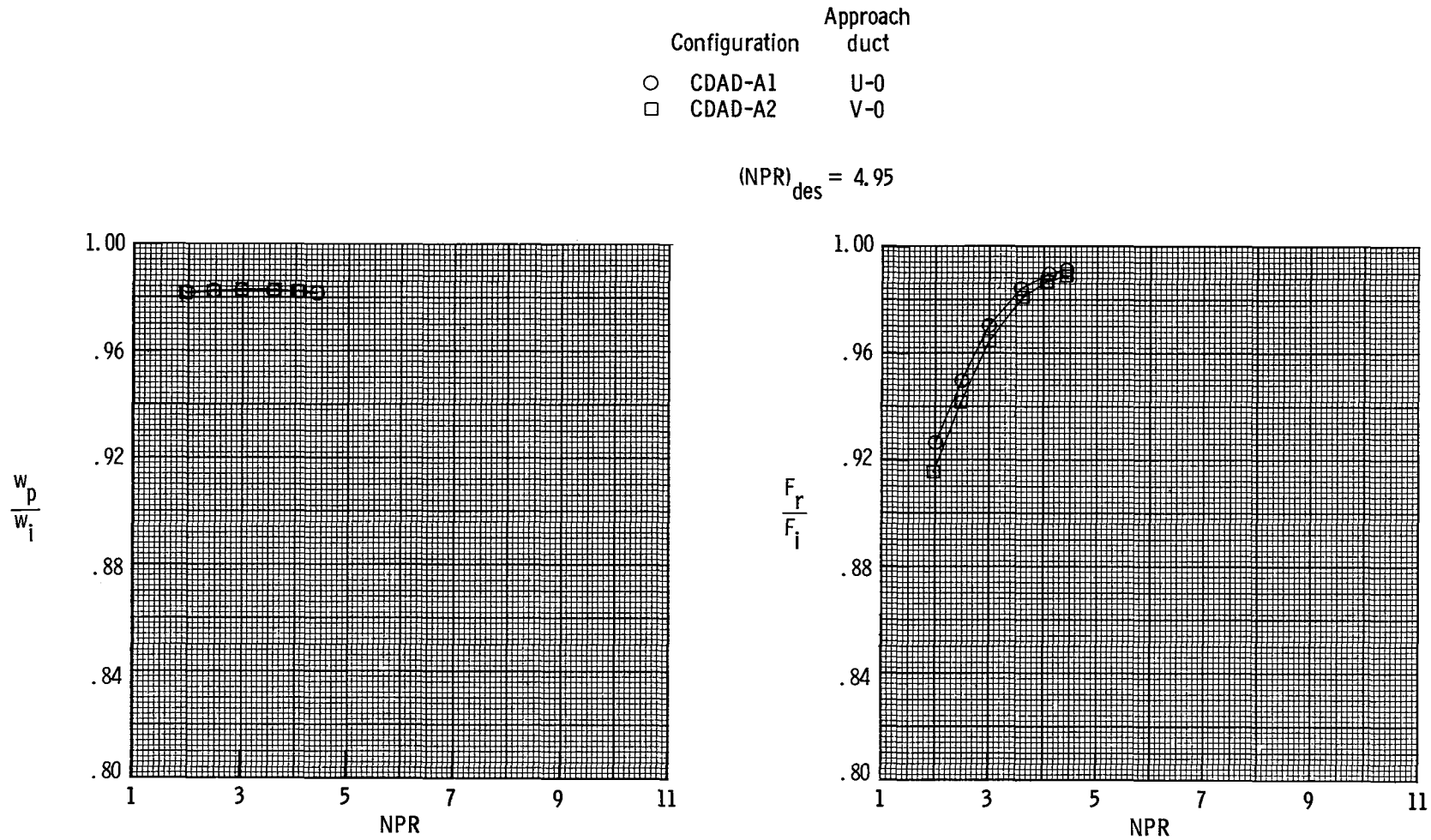

Figure 22.- Effect of approach-duct geometry on nozzle discharge coefficient and resultant thrust ratio for A/B-power CDAD configurations. $\delta_{v,p} = 0°$.

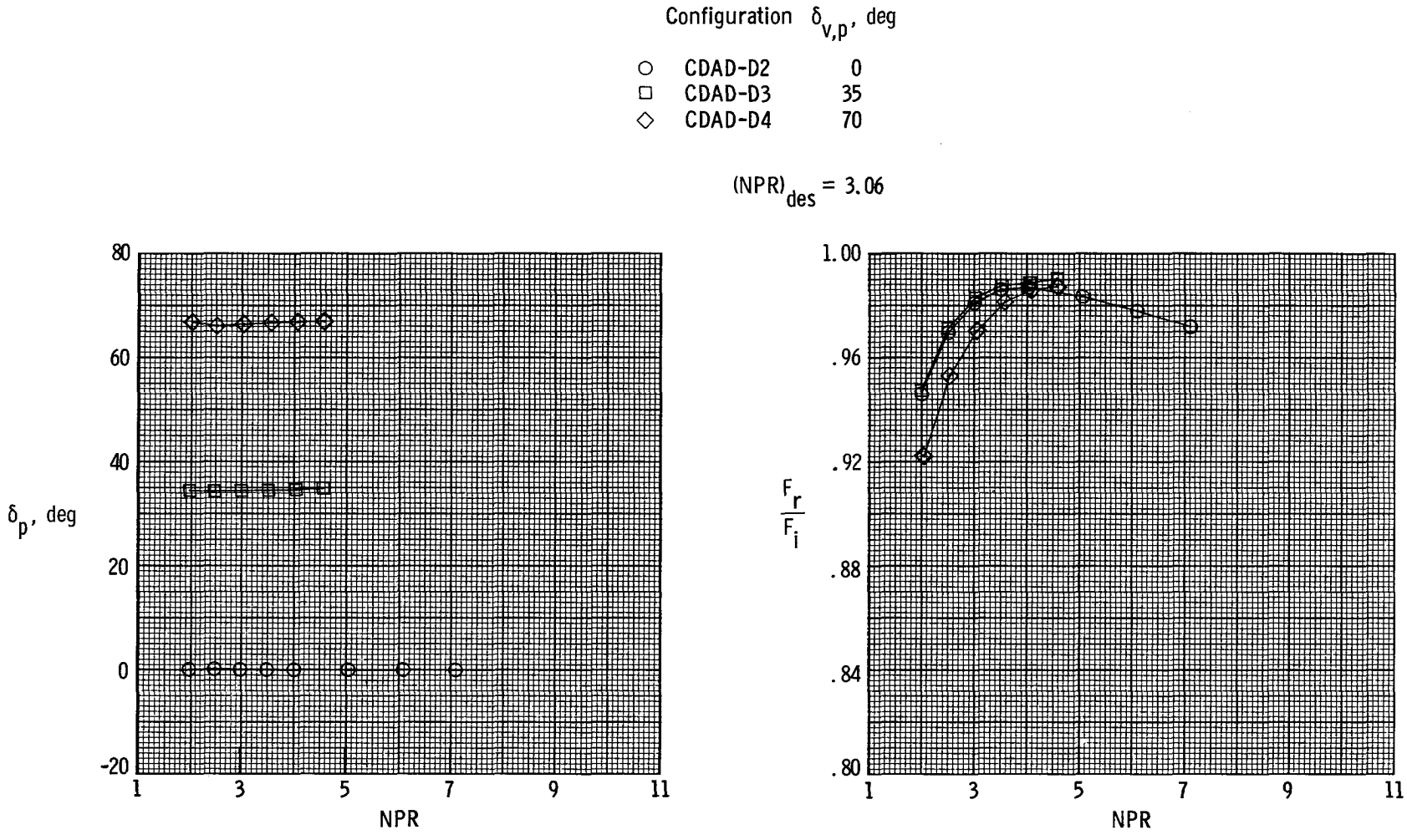

Figure 23.- Effect of pitch thrust vectoring (through approach-duct deflection) on resultant pitch thrust-vector angle and resultant thrust ratio for dry-power CDAD configurations with approach duct V.

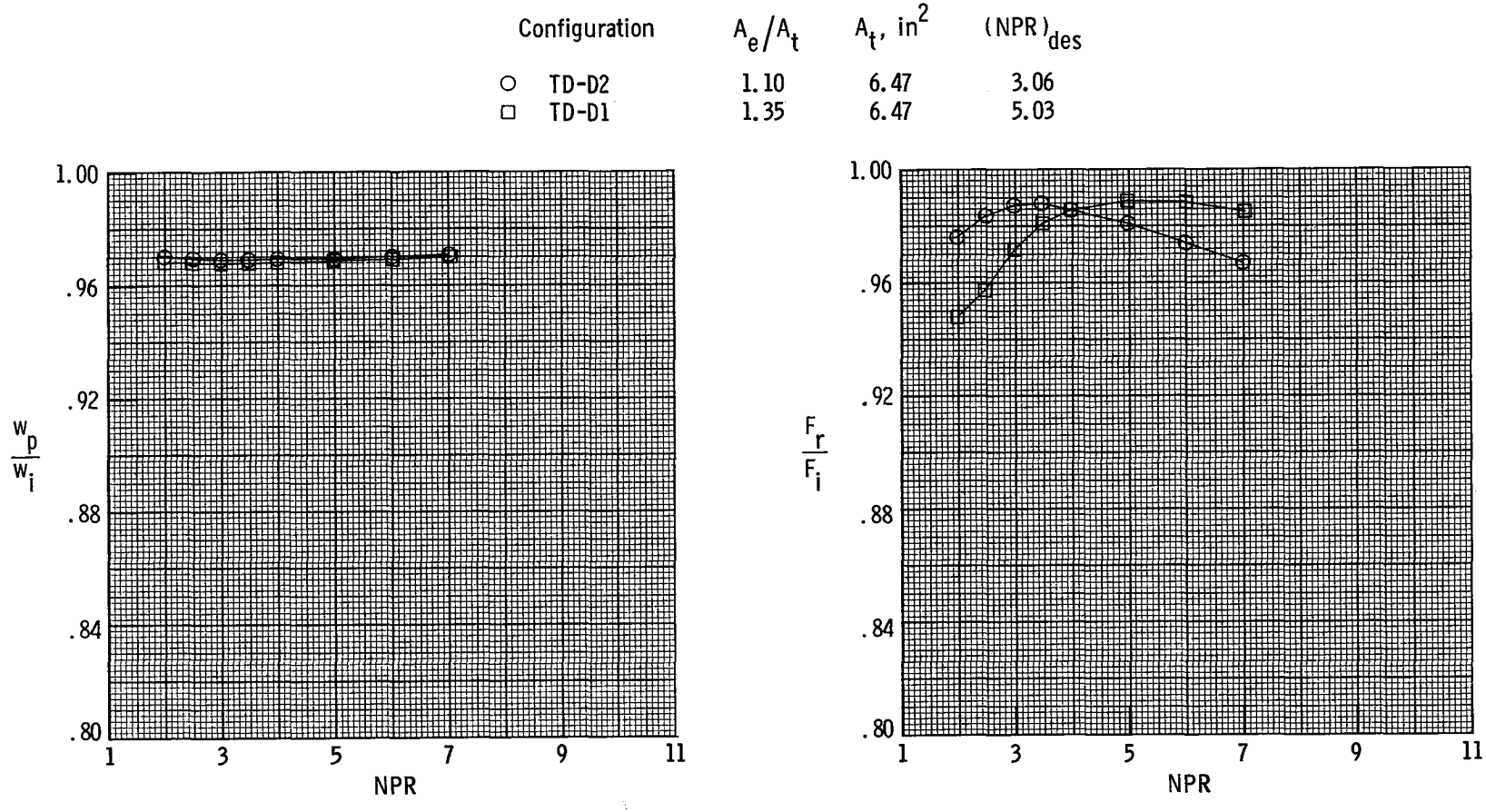

Figure 24.- Effect of nozzle expansion ratio on nozzle discharge coefficient and resultant thrust ratio for dry-power 2-D C-D nozzle configurations. $\delta_{v,p} = 0°$.

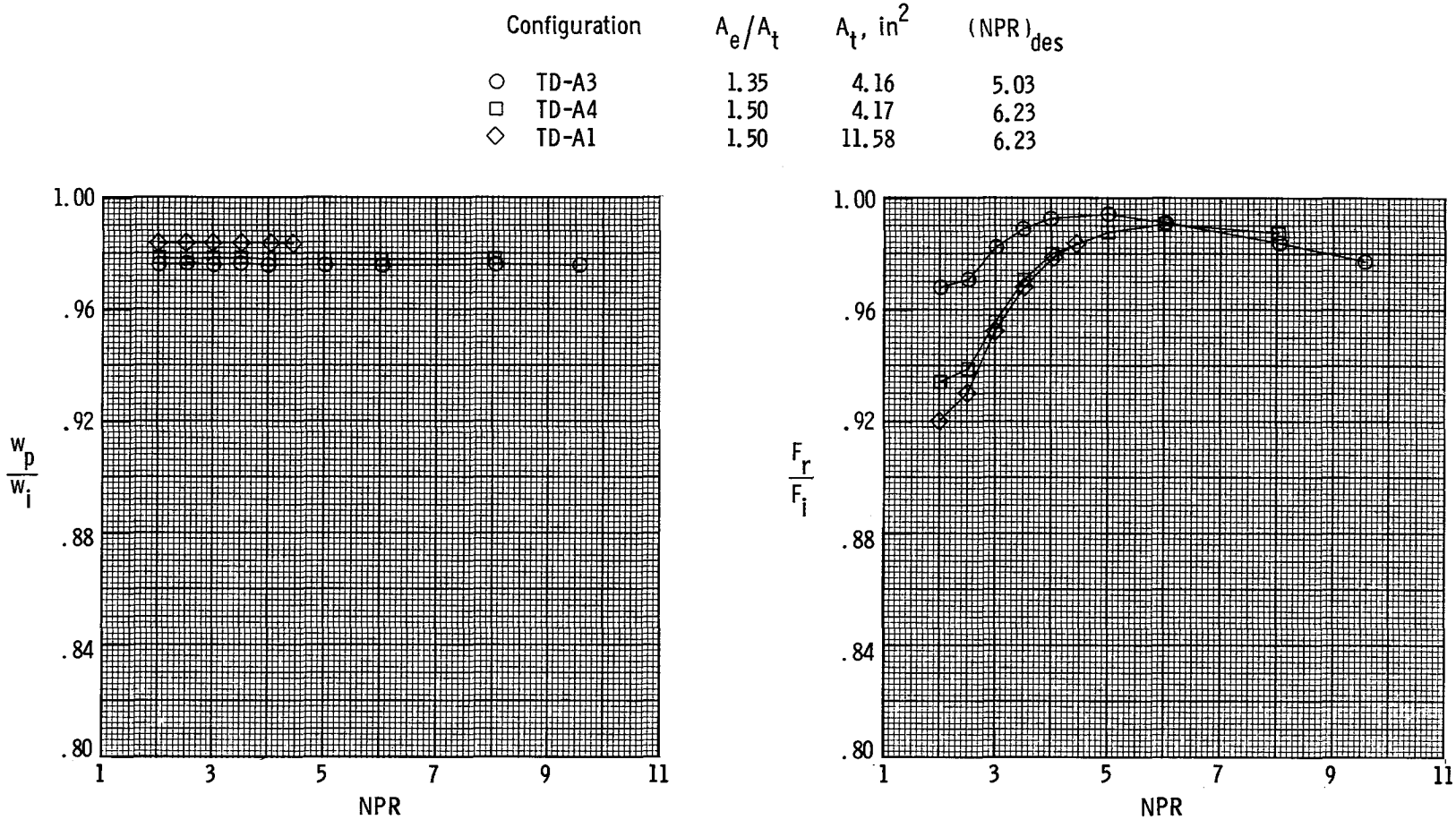

Figure 25.- Effect of nozzle expansion ratio on nozzle discharge coefficient and resultant thrust ratio for A/B-power 2-D C-D nozzle configurations. $\delta_{v,p} = 0°$.

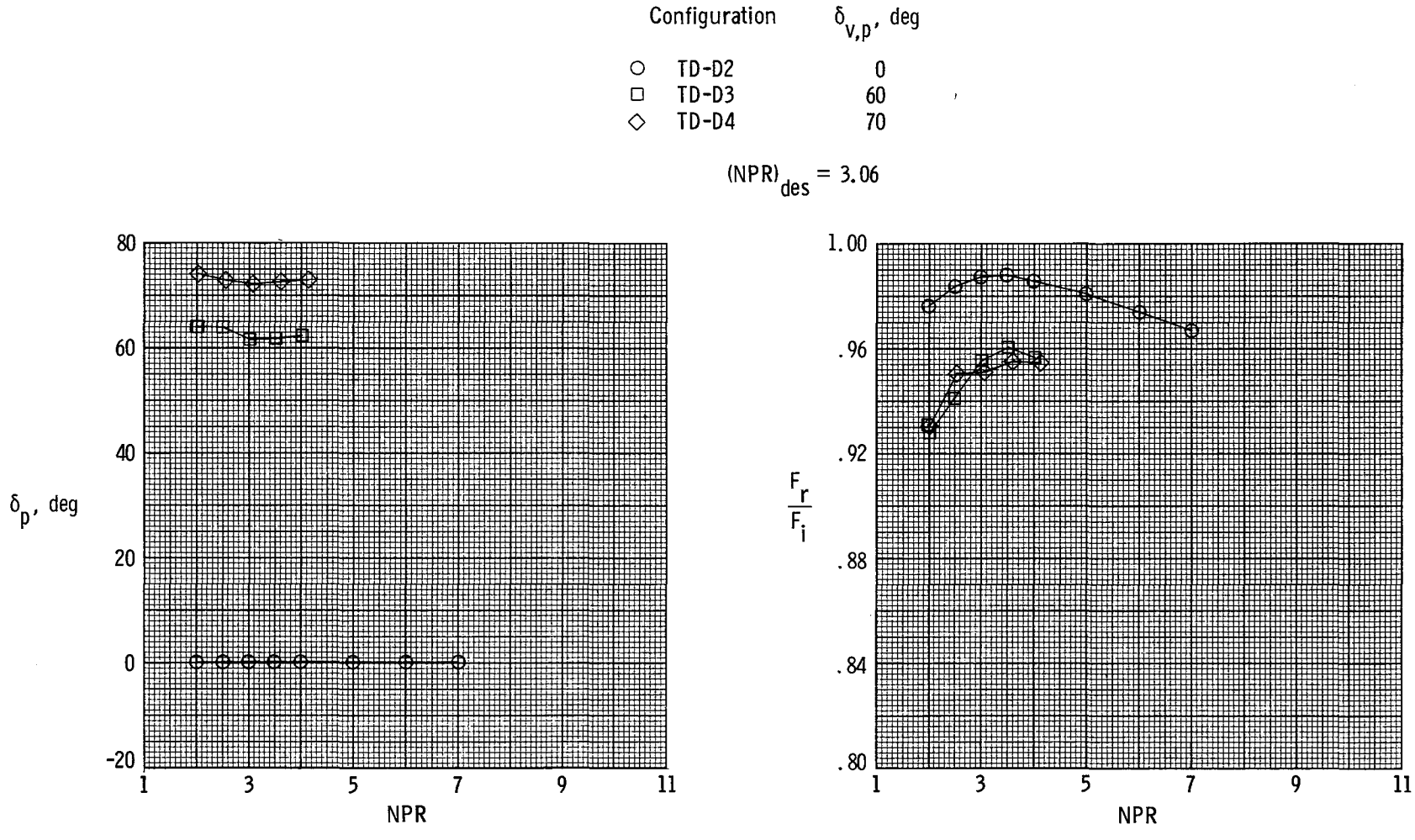

Figure 26.- Effect of pitch thrust vectoring on resultant pitch thrust-vector angle and resultant thrust ratio for dry-power 2-D C-D nozzle configurations.

1. Report No.	2. Government Accession No.	3. Recipient's Catalog No.
NASA TP-2559		

4. Title and Subtitle	5. Report Date
Static Investigation of Two STOL Nozzle Concepts With Pitch Thrust-Vectoring Capability	April 1986
	6. Performing Organization Code: 505-62-91-01
7. Author(s): Mary L. Mason and James R. Burley II	8. Performing Organization Report No.: L-16052
9. Performing Organization Name and Address: NASA Langley Research Center, Hampton, VA 23665-5225	10. Work Unit No.
	11. Contract or Grant No.
12. Sponsoring Agency Name and Address: National Aeronautics and Space Administration, Washington, DC 20546-0001	13. Type of Report and Period Covered: Technical Paper
	14. Sponsoring Agency Code

15. Supplementary Notes

16. Abstract

A static investigation of the internal performance of two short take-off and landing (STOL) nozzle concepts with pitch thrust-vectoring capability has been conducted. An axisymmetric nozzle concept and a nonaxisymmetric nozzle concept were tested at dry and afterburning power settings. The axisymmetric concept consisted of a circular approach duct with a convergent-divergent nozzle. Pitch thrust vectoring was accomplished by vectoring the approach duct without changing the nozzle geometry. The nonaxisymmetric concept consisted of a two-dimensional convergent-divergent nozzle. Pitch thrust vectoring was implemented by blocking the nozzle exit and deflecting a door in the lower nozzle flap. The test nozzle pressure ratio was varied up to 10.0, depending on model geometry. Results indicate that both pitch vectoring concepts produced resultant pitch vector angles which were nearly equal to the geometric pitch deflection angles. The axisymmetric nozzle concept had only small thrust losses at the largest pitch deflection angle of 70°, but the two-dimensional convergent-divergent nozzle concept had large performance losses at both of the two pitch deflection angles tested, 60° and 70°.

17. Key Words (Suggested by Authors(s))	18. Distribution Statement
Axisymmetric nozzles Nonaxisymmetric nozzles Thrust vectoring Internal performance	Unclassified - Unlimited Subject Category 02

19. Security Classif.(of this report)	20. Security Classif.(of this page)	21. No. of Pages	22. Price
Unclassified	Unclassified	55	A04

For sale by the National Technical Information Service, Springfield, Virginia 22161

NASA-Langley, 1986

NASA

POSTMASTER: If Undeliverable (Section 158 Postal Manual) Do Not Return